Experimental and Theoretical Investigations of the Inelastic and Reactive Scattering Dynamics of O(^3P) Collisions with Ethane[†]

Donna J. Garton and Timothy K. Minton*

Department of Chemistry and Biochemistry, Montana State University, Bozeman, Montana 59717

Wenfang Hu and George C. Schatz*

Department of Chemistry, Northwestern University, Evanston, Illinois 60208-3133

Received: January 14, 2009; Revised Manuscript Received: February 26, 2009

Detailed experimental and theoretical investigations have been carried out for the reaction of O(^3P) with CH_3CH_3 at collision energies in the range of 80−100 kcal mol^{-1}. Experiments were performed on a crossed molecular beams apparatus with a laser breakdown source (which produces beams of O(^3P) with average velocities of 6.5 to 8.5 km s^{-1}) and a pulsed supersonic source of CH_3CH_3 having an average velocity of ~0.8 km s^{-1}. A rotatable quadrupole mass spectrometer allowed universal detection, with angular and velocity resolution of products scattering from the crossing region of the two reagent beams. Theoretical calculations were carried out in two stages, (1) electronic structure calculations to characterize the stationary points associated with the title reaction and (2) direct dynamics calculations employing the MSINDO semiempirical Hamiltonian and density functional theory (B3LYP/6-31G**). The dynamics of O-atom inelastic scattering and H-atom abstraction to form OH + C_2H_5 were clearly revealed by the experiment and were matched well by theory. Both of these processes favor high-impact parameters, with most of the available energy going into translation, indicating a stripping mechanism for H-atom abstraction. H-atom abstraction was the dominant reactive pathway, but H-atom elimination to form OC_2H_5 + H was also inferred from the experimental results and observed in the theoretical calculations. This reaction proceeds through small-impact-parameter collisions, and most of the available energy goes into internal excitation of the OC_2H_5 product, which likely leads to secondary dissociation to H_2CO + CH_3 or CH_3CHO + H. A relative excitation function for the H-atom elimination channel was also measured and compared to a calculated absolute excitation function. The theoretical calculations also identified several additional reaction pathways with low relative yields, including C−C bond breakage to form OCH_3 + CH_3. Interference from OC_2H_5 decomposition products in the experiment inhibited the unambiguous observation of the low-yield reaction pathways that were identified by theory, although an upper limit for the relative yield of C−C bond breakage was determined.

I. Introduction

Multichannel reactions, important in many radical−molecule or radical−radical systems,[1] are not typically a concern in O(^3P) reactions with alkanes because only the H-atom abstraction reaction to form OH is available at commonly encountered temperatures or collision energies, such as those found in hydrocarbon combustion processes.[2] In extreme environments, however, such as those created by the high velocities of space vehicles that travel through Earth's outer atmosphere, high collision energies involving O(^3P) are the norm.[3] Hyperthermal collisions between ambient O(^3P) and spacecraft surfaces or exhaust gases may have center-of-mass (c.m.) collision energies of tens of kilocalories per mole, perhaps even exceeding 100 kcal mol^{-1}. (For a typical relative velocity of 8 km s^{-1}, the collision energy between O atoms and the small hydrocarbon molecule, ethane, would be 80 kcal mol^{-1}.) These high collision energies exceed the barriers to many reactive processes, opening up multiple reactive channels, for example, in collisions of O(^3P) with gaseous and surface hydrocarbons.[4] When O(^3P) atoms collide with alkane molecules at collision energies above ~45 kcal mol^{-1}, H-atom elimination and C−C bond-breaking reactions may occur.[5−9]

The O(^3P) + CH_3CH_3 collision system has been treated as a model for studies of hyperthermal O-atom reactions with hydrocarbons. Except for a preliminary report on experiments with this system at hyperthermal collision energies,[8] the work to date has come from theory. Massa and co-workers[10] used ab initio molecular orbital calculations to investigate the possibility of chain breaking in hyperthermal collisions of O(^3P) with several small alkanes, and they calculated transition-state energies and structures for the reaction, O(^3P) + CH_3CH_3 → OCH_3 + CH_3. They found that the O atom is aligned with the two carbon atoms in the transition state and that the reaction barrier is probably 40−50 kcal mol^{-1}. Our groups expanded on this study and considered additional transition states.[11] We also performed direct dynamics simulations to calculate cross sections and analyze the dynamics of the various reaction pathways for a wide range of collision energies. The two dominant reaction pathways were found to be (1) hydrogen-atom abstraction to form OH and C_2H_5 and (2) hydrogen-atom elimination to form OC_2H_5 + H. Our work showed that the C−C bond-breakage reaction described by Massa and co-workers was a very minor channel and was similar in cross section to a reaction leading to H_2O + CH_3CH. One transition

---

[†] Part of the "George C. Schatz Festschrift".

* To whom correspondence should be addressed.

10.1021/jp900412w CCC: $40.75

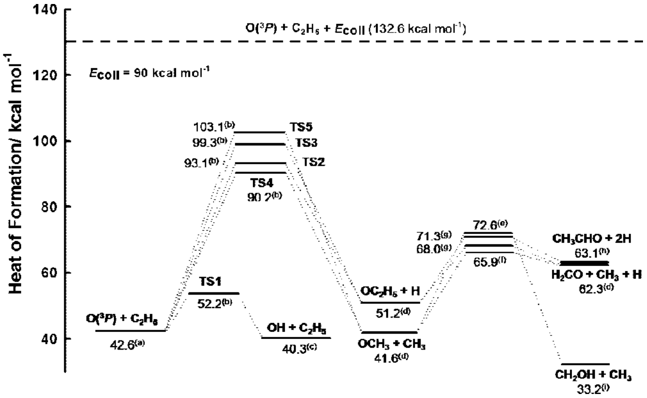

Figure 1. Enthalpy (at 0 K) diagram for various possible reaction channels in the reaction of O(^3P) with CH_3CH_3. The numbers are in kcal mol^{-1}. The horizontal line at the top indicates the available energy for the reactions under our experimental conditions, where the nominal center-of-mass collision energy was 90 kcal mol^{-1}. (a) Ref 35. (b) Ref 36. (c) Ref 37. (d) Ref 38. (e) Ref 39. (f) Ref 40. (g) Ref 41. (h) Ref 42. (i) Ref 43.

state was found for the H-atom abstraction channel, two for the H-atom elimination channel, and two for the C−C bond-breakage channel. Barriers for each stationary point were calculated at the CCSD(T)/AUG-cc-pVTZ level, and they ranged from 9.5 kcal mol^{-1} for the H-atom abstraction pathway to 60.5 kcal mol^{-1} for the highest-energy C−C bond-breakage transition state. The lowest pathway other than H-atom abstraction was found to be H-atom elimination, which was calculated to have a barrier of 50.5 kcal mol^{-1}. Hase and co-workers[12] carried out a similar study of O + CH_3CH_3 reactions at a collision energy of 115 kcal mol^{-1}. They first developed two PM3-SRP models for the potential energy surface and then employed these models in direct dynamics simulations, integrating the trajectories for a long enough time to investigate secondary dissociation of internally excited primary products. Their findings for the energetics and dynamics of the primary reaction pathways was similar to those found by work in our groups, but the new work by Hase and co-workers revealed a rich array of secondary processes that may take place subsequent to or almost simultaneous with the primary reactions. The complexity of the secondary chemistry was probably amplified by the relatively high collision energy used in their calculations. The energy level diagram in Figure 1 illustrates reaction energies and barriers for the three main primary reaction pathways and for the secondary pathways that are believed to be most important for collision energies less than 100 kcal mol^{-1}.

The experimental description of the dynamics of the O(^3P) + CH_3CH_3 model hyperthermal reactive system has lagged the theory because of the difficulty of achieving the relevant high collision energies and the complications inherent in studying multichannel reaction dynamics.[1] Nevertheless, we have conducted a crossed-beams study of this reaction at a collision energy of 90 kcal mol^{-1}, in which we have clearly identified two primary reaction pathways, leading to OH + C_2H_5 and OC_2H_5 + H, and have investigated a third (C−C bond breakage). In addition, we have studied the inelastic scattering dynamics of O(^3P) and CH_3CH_3 in detail. In parallel, we have performed additional theoretical calculations in order to derive dynamical quantities that may be compared directly to the experimental results. The analysis of the experimental data was greatly enhanced by the concomitant calculations, which have added insight beyond what was accessible in the experiment. A full report of our combined experiment/theory study is presented below.

II. Theoretical Details

A. Quantum Chemistry Calculations. Prior to calculations of the quasiclassical trajectories (QCT), stationary points along three basic reactive pathways (i.e., H-atom abstraction, H-atom elimination, and C−C bond breakage) were characterized by electronic structure calculations utilizing the MSINDO semiempirical Hamiltonian[13] and a higher-level density functional theory (DFT) method B3LYP[14] with a 6-31G** basis set. The transition-state (TS) structures calculated by these methods and by UMP2/cc-pVTZ ab initio calculations[11] may be seen in Supporting Information (Figure SI-1). The abstraction TS exhibits the typical near-collinear O−H−C arrangement, which is also found for many H-atom abstraction reactions such as O(^3P) with hydrogen, methane, and propane.[2] Both the H-atom elimination and C−C bond-breakage reactions have two saddle point geometries. In one of them, the incoming oxygen atom is largely in a line with the carbon atom and the departing species (the H atom or the methyl radical). In the other, O adds to the carbon atom at a much more bent angle with respect to the departing H or CH_3.

Reaction and transition-state energies for three primary and several secondary reactions are shown in Figure 1. The transition-state energies for the primary reactions were taken from zero-point-corrected CCSD(T)/cc-pVTZ calculations. Also included are results from Hase and co-workers who carried out very high level electronic structure calculations for O(^3P) reactions with methane and ethane.[15] For O(^3P) + ethane, they considered the H-atom abstraction and C−C bond-breakage channels, as well as secondary reactions involving the OH radical. The highest level of theory that they used was MRCI+Q single-point energies extrapolated to the complete basis set limit (CBL) at CASSCF/cc-pVTZ or CASPT2/cc-pVTZ optimized geometries.

Table 1 contains the reaction and transition-state energies involved in the three primary reactions at different levels of theory, along with a comparison with the available experimental values. Although the MSINDO reaction energies deviate greatly from those obtained using the other methods, being much too exothermic, the barriers to reaction and especially their relative ordering are in general agreement with all of these methods. The abstraction reaction has the lowest barrier, while H-atom elimination and C−C bond breakage have much higher barriers that are similar to each other. The MRCI+Q/CBL energies, being the most accurate calculations done for this system so far, give the best agreement with experiment but are consistently higher than the experimental values by 0.9−2.4 kcal mol^{-1}. Second to MRCI+Q calculations in accuracy are CCSD(T)/cc-pVTZ energies, which differ from available experimental enthalpies and barriers by even larger amounts (3.0−5.4 kcal mol^{-1}). The B3LYP calculations underestimate the abstraction barrier by ~5.5 kcal mol^{-1} as compared to an estimate based on experimental data. From the performance of the B3LYP and CCSD(T) calculations, we infer that the H-atom elimination and C−C bond-breakage barrier heights should be between the B3LYP/6-31G** and CCSD(T)/cc-pVTZ values.

B. Reaction Dynamics Calculations. The O(^3P) + CH_3CH_3 reaction has been investigated with the QCT method in the scheme of direct dynamics electronic structure calculations where energies and forces are computed as the trajectory evolves on the MSINDO or B3LYP/6-31G** surface. For calculating the MSINDO and B3LYP trajectories, we have interfaced MSINDO and the Q-Chem computer program[16] with a molecular dynamics code utilizing a standard fifth-order predictor, sixth-order corrector integrator[17] to propagate the equations of

TABLE 1: Energies of the Stationary Points Associated with Three $O(^3P) + CH_3CH_3$ Reactions[a,b]

species	MSINDO[c]	B3LYP/6-31G**	CCSD(T)/cc-pVTZ[d]	MRCI+Q/CBL	expt.[g]
$O(^3P) + C_2H_6$	0	0	0	0	0
$OH + C_2H_5$	−18.9 (−13.6)	−0.3 (4.1)	0.97 (5.14)	−1.4 (2.7)[e]	−2.3
$H + OC_2H_5$	−8.3 (−1.56)	7.7 (14.2)	14.0 (19.1)		8.6
$CH_3 + OCH_3$	−17.9 (−11.8)	−2.5 (1.74)	3.04 (7.9)	1.1 (6.3)[f]	−1.0
TS1 (abstraction)	7.1 (11.8)	1.14 (5.5)	9.6 (13.2)	9.0 (13.0)[e]	6.6[h]
TS2 (H elimination)	38.5 (43.3)	42.8 (46.4)	50.5 (53.7)		
TS3 (H elimination)	37.1 (41.3)	47.7 (52.0)	56.66 (60.2)		
TS4 (C−C breakage)	37.3 (39.0)	38.4 (40.9)	47.55 (49.26)	46.9 (50.2)[f]	
TS5 (C−C breakage)	45.7 (49.4)	51.4 (53.0)	60.5 (63.5)		

[a] Energies are in kcal mol^{-1}. [b] Values in parentheses are classical energies. Energies obtained after correction for the zero-point energies (plain values) can be compared with experiment. [c] Note that the zero-point energies reported in the MSINDO outputs are scaled so that they are significantly smaller than what would correspond to the actual curvature of the potential surface. We have used the actual values of the zero-point energies as obtained from the MSINDO Hessian matrices. [d] Values taken from ref 11. [e] MRCI+Q(8,8)/CBL single-point energies at CASPT2(8,8)/cc-pVTZ optimized geometries. The readers are referred to ref 15 for calculation details. [f] MRCI+Q(4,4)/CBL single-point energies at CASSCF(4,4)/cc-pVTZ optimized geometries. The readers are referred to ref 15 for calculation details. [g] From values in Figure 1. [h] From the evaluation by Troya et al. in ref 11.

motion. The self-consistent field (SCF) unrestricted Hartree−Fock (UHF) technique was employed. Batches of 10000 MSINDO trajectories were run at $E_{coll} = 34.6$, 60.0, 74.9, and 90.0 kcal mol^{-1}. For B3LYP, 1000 trajectories were calculated at $E_{coll} = 60.0$ and 90.0 kcal mol^{-1} in consideration of the much higher computational cost. The MSINDO trajectories were started at an initial c.m. separation of 12 a_0 and stopped at approximately the same distance for the product pair, whereas for the initialization and completion of the B3LYP trajectories, we used a value of 15 a_0. We used a shorter initial and final c.m. separation in calculating the MSINDO trajectories because of problems with convergence of the MSINDO calculations at large distances. For the same reason, the integration time step was 5 au (∼0.12 fs) in the MSINDO calculations and 10.0 au for the B3LYP calculations. The impact parameter was sampled between 0 and 7.5 a_0 for both surfaces. In the analysis of the trajectory output, we discarded those trajectories whose initial and final total energy difference exceeded 2 kcal mol^{-1}, which amounted to 43 out of the total 10000 trajectories run at $E_{coll} = 90$ kcal mol^{-1} on the MSINDO surface. No B3LYP trajectories had to be discarded due to their much better energy conservation. The QCT trajectories were started with the CH_3CH_3 molecule prepared in its ground electronic and rovibrational states. Specifically, we ran an intramolecular trajectory (called the "root" trajectory) starting from the equilibrium geometry of C_2H_6 with a kinetic energy corresponding to the zero-point energy (ZPE) in each normal mode. The root trajectory was integrated for many vibrational periods, and the phase of the vibrational motion was sampled uniformly over this time interval. Then, the impinging O atom was placed randomly around the vibrating molecule at a fixed c.m. separation, a randomly sampled impact parameter, and a predetermined relative translational energy between $O(^3P)$ and C_2H_6. As we used classical mechanics, the products may have smaller energies than their ZPEs. In such cases, we "rounded up" the fragment's energy to the ZPE. Although it is possible for reaction products to be sufficiently internally excited to undergo secondary dissociation (and such secondary processes were occasionally observed even on the time scale of the calculations, <0.3 ps), the analysis was limited to a description of the dynamics of the primary reaction steps.

Excitation and opacity functions may be found in Supporting Information (Figures SI-2, SI-3, and SI-4) and are summarized here. The most important reaction paths lead to the products, $OH + C_2H_5$, $OC_2H_5 + H$, and $OCH_3 + CH_3$. (Note that there were too few trajectories for the C−C bond-breakage reaction to allow for a meaningful opacity function for this reaction.) The abstraction reaction, being the lowest barrier process, dominates over all other channels throughout the entire energy range studied, from 34.6 to 90 kcal mol^{-1}. On the other hand, the H-atom elimination cross section steadily increases from its threshold and becomes more than half of the magnitude of the abstraction reaction cross section, according to the MSINDO calculations. This increase was predicted to continue up to a collision energy of 132.6 kcal mol^{-1} (not shown in Supporting Information), but the cross section for H-atom elimination still remains lower than that for the abstraction reaction. Although the barriers to C−C bond breakage are fairly close to those for H-atom elimination, the C−C bond-breakage reaction cross section increases noticeably slower with collision energy than the cross section for H-atom elimination. This difference is expected based on statistical grounds because the possibility of a hydrogen atom being replaced (i.e., H-atom elimination) is three times higher than the probability of a methyl group being replaced (i.e., C−C bond breakage) when O collides with one of the carbon atoms in ethane. Comparing the MSINDO and B3LYP results, we note that there is a much larger cross section gap between the abstraction reaction and the other channels on the B3LYP than on the MSINDO surface. The very low energy barrier to abstraction predicted by B3LYP suggests an overestimation of the reactivity for this channel on the B3LYP surface. Indeed, the experimental product yield for H-atom abstraction at $E_{coll} = 90$ kcal mol^{-1} is not as high as that calculated from the B3LYP trajectories (Table 2).

We summarize in Table 2 the relative product yields for the primary reaction pathways of the $O(^3P) + CH_3CH_3$ reaction that have been identified by our QCT calculations on the MSINDO and B3LYP surfaces. Note that some minority products, such as $^3CH_3CH + H_2O$ and $^3CH_2CH_2 + H_2O$, have been observed in the calculations and that $^3CH_3CH + H_2O$ may be produced with comparable or even higher probability than $CH_3 + OCH_3$, especially on the B3LYP surface. The theoretical relative yields are based on the total cross section given by

$$\sigma_{tot} = \frac{\pi}{p^2} \sum_{i=1}^{N_{tot}} \frac{(2l_i + 1)l_{max}}{N_{tot}}$$

where $p = (2\mu E_{trans})^{1/2}$ is the momentum of the reactant system and $l_i = b_i p$ is the angular momentum of trajectory i; $l_{max} = b_{max}p$, where b_{max} is the maximum impact parameter sampled by the trajectories ($b_{max} = 7.5\ a_0$). The integral cross section for each reaction channel is

$$\sigma_r = \frac{\pi}{p^2} \sum_{i=1}^{N_r} \frac{(2l_i + 1)l_{\max}}{N_{\text{tot}}}$$

where the sum is over all of the trajectories that are assigned to each reaction channel. The branching fraction for each reaction channel thus is $(\sigma_r/\sigma_{\text{tot}}) \times 100\%$.

Further detailed analyses of the trajectory output, such as the opacity functions and product angular and energy distributions, when combined with experimental observations help elucidate the atomistic-scale mechanisms through which the inelastic and reactive scattering of the reactant molecules occurs. The results will be discussed in sections IV and V.

III. Experimental Details

Experiments were performed with the use of a crossed molecular beams apparatus, as describer earlier.[18,19] Pulsed beams of neat CH_3CH_3 traveling ~800 km s^{-1}, created with the use of a piezoelectric pulsed valve,[20] passed through a 2 mm skimmer into a differential pumping region before entering the main scattering chamber (held at ~10^{-7} Torr) through a 2.5 mm diameter aperture. No ethane dimers were detected in the beam when it was probed directly with a mass spectrometer detector. The ethane beam was crossed with a pulsed, hyperthermal beam traveling at a nominal velocity of 8 km s^{-1} and containing ~70% ground-state oxygen atoms ($^3P_{0,1,2}$) and ~30% ground-state O_2 ($^3\Sigma_g^-$).[21,22] The hyperthermal beam was produced with laser-breakdown source based on the original design of Caledonia et al.[23] The hyperthermal oxygen beam pulse passed through a relatively large aperture (7 mm diameter) into a differential pumping region and then passed through a 3 mm diameter skimmer before reaching the main scattering chamber. A narrowed range of velocities was selected from the overall beam pulse with the use of a synchronized chopper wheel, rotating at 300 or 400 Hz.[18] Products that scattered from the crossing point of the two beams traveled 33.7 cm to the Brink-type electron bombardment ionizer.[24] Once ionized, the products were mass selected with a quadrupole mass filter and detected by a Daly-type ion counter.[25] Number density distributions of mass-selected species were collected as a function of their arrival time in the ionizer. Such number density distributions, $N(t)$, are commonly referred to as time-of-flight (TOF) distributions. The entire detector rotates around the crossing point of the two beams, allowing TOF distributions to be acquired at a variety of scattering angles with respect to the hyperthermal beam. The range of detector angles used for data collection in this study was 7.5−50° and is shown as the gray shaded region on the Newton diagram in Figure 2.

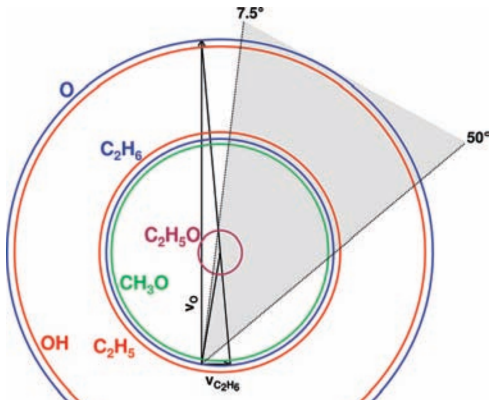

Figure 2. Newton diagram for the O(^3P) + CH_3CH_3 reaction at E_{coll} = 90 kcal mol^{-1}, where O has a velocity of 8450 m s^{-1} and CH_3CH_3 has a velocity of 800 m s^{-1}. The laboratory angular range accessible in the experiment is shown as the shaded region, where the laboratory angles shown are with respect to the O-atom beam direction. The radii of the blue circles represent the velocities of elastically scattered products; the scattered ethane (inner blue circle) and scattered oxygen atoms (outer blue circle) are shown. The radii of the red circles represent the maximum possible velocities of the H-atom abstraction products, in which the products formed are C_2H_5 (inner circle) and OH (outer circle). The radius of the purple circle represents the maximum possible velocity of the ethoxy (OC_2H_5) product of the H-atom elimination reaction. The green circle represents the maximum possible velocity of the OCH_3 product in the C−C bond-breakage reaction. The nominal angle of the center-of-mass velocity vector with respect to the O-atom beam direction is ~10°.

In order to determine oxygen-atom beam velocity distributions, the detector was rotated such that the detection and hyperthermal beam axes coincided (laboratory angle, Θ, of 0°), and TOF distributions were collected as a function of the flight time from the nozzle to the ionizer. Velocity distributions were derived from the TOF distributions. Three different average O-atom beam velocities were used to obtain dynamical information, 8.40 km s^{-1} (300 Hz chopper wheel), 8.44 km s^{-1} (400 Hz chopper wheel), and 8.50 km s^{-1} (400 Hz chopper wheel). Velocity widths (fwhm) of the beams were 530 m s^{-1} when the 300 Hz chopper wheel was used and 440 m s^{-1} with the 400 Hz chopper wheel. The nominal c.m. collision energies with these three O-atom beams ranged from 89 to 91 kcal mol^{-1}. The fraction of O_2 in the beams varied from 20 to 40%, depending on the beam conditions, with higher velocity beams generally containing a lower fraction of O_2.

TOF distributions were collected for a survey of mass-to-charge ratios at a laboratory angle of 10°. These TOF distributions may be seen in Supporting Information (Figure SI-5). Many of the TOF distributions collected at lower mass-to-charge ratios could contain signals from multiple reaction channels, as a result of product fragmentation in the ionizer. TOF distributions were also collected at several laboratory angles for m/z = 16 (O^+), 17 (OH^+), 27 ($C_2H_3^+$), 29 ($C_2H_5^+$, CHO^+), 30 ($C_2H_6^+$, CH_2O^+), 32 (O_2^+), and 43 ($C_2H_3O^+$). TOF distributions collected

TABLE 2: Theoretical Relative Cross Sections (Branching Fractions) Based on the MSINDO (Plain Values) and the B3LYP/6-31G (Values in Parentheses) Calculations for the Major Reaction Pathways at Various Collision Energies**[a]

E_{coll}	34.6 kcal mol^{-1}	60 kcal mol^{-1}	74.9 kcal mol^{-1}	90 kcal mol^{-1}
inelastic scattering	92%	86.8% (85.2%)	83.3%	80.7 ± 1.0% (81.6 ± 3.3%) [85%]
OH + C_2H_5	7.9%	10.6% (13.9%)	10.7%	10.8 ± 0.3% (14.7 ± 0.9%) [10%]
OC_2H_5 + H	0%	2.4% (0.13%)	5.1%	7.1 ± 0.2% (2.7 ± 0.3%) [≥4%]
OCH_3 + CH_3	0%	0.2% (0.03%)	0.69%	0.9 ± 0.04% (0.28 ± 0.09%) [≤1%]
$^3CH_3CH$ + H_2O	0.03%	0.1% (0.33%)	0.18%	0.27 ± 0.06% (0.59 ± 0.20%)
$^3CH_2CH_2$ + H_2O	0%	0% (0.4%)	0%	0% (0.2 ± 0.1%)

[a] The branching fraction for OC_2H_5 + H includes all trajectories that first produced OC_2H_5, even if it underwent subsequent secondary dissociation. Current experimental measurements are presented in brackets for the 90 kcal mol^{-1} collision energy.

at m/z = 16 were corrected by subtracting 11% of the TOF distribution collected at m/z = 32 because this fraction of the signal at m/z = 16 comes from dissociative ionization of O_2. TOF distributions were collected with the 8.44 km s^{-1} O-atom beam for m/z = 16, 17, and 32 in 5° increments from 10 to 50° and with the 8.50 km s^{-1} beam in 10° increments from 10 to 50° for m/z = 27, 29, and 30. TOF distributions for m/z = 43 were collected in 2.5° increments from 7.5 to 20° with the 8.40 km s^{-1} O-atom beam. A forward convolution approach, which has been described in detail elsewhere,[18,26−29] was carried out in order to derive c.m. quantities, such as translational energy distributions, $P(E)$, and angular distributions, $T(\theta)$, from the laboratory data.

The small c.m. velocities of the ethoxy (OC_2H_5) product and its consequent scattering in a relatively confined region of velocity space (see Figure 2) permitted an investigation of the scattered flux of the ethoxy product as a function of collision energy. TOF distributions were collected at laboratory angles of 9.5−11.5° for five different collision energies. Average O-atom beam velocities (and corresponding collision energies in kcal mol^{-1}) used for this study were 7.41 (69), 7.54 (72), 7.99 (80.4), 8.40 (89), and 8.79 km s^{-1} (97). The variation in beam velocity was achieved by adjusting the timing between the pulsed O-atom beam and the velocity selector (chopper) wheel spinning at 400 Hz. TOF distributions were collected for m/z = 43 ($OC_2H_3^+$) with each O-atom beam velocity. The angle of the c.m. velocity vector relative to the O-atom beam velocity vector changes slightly with beam velocity (and the resultant collision energy) and thus varied from 11.5° for the 7.41 km s^{-1} beam to ~9.5° for the 8.79 km s^{-1} beam.

IV. Results and Analysis

A. Inelastic Scattering of O Atoms. TOF distributions for m/z = 16 at five laboratory angles are shown as yellow circles in Figure 3. The laboratory angular distribution, or integrated TOF signal as a function of laboratory angle, $N(\Theta)$, for oxygen-atom inelastic scattering is shown as black solid circles in Figure 4. The blue curves in Figures 3 and 4 are the forward-convolution simulations to the data based on the c.m. translational energy and angular distributions shown as blue curves in Figure 5. The translational energy distribution, which along with the angular distribution was derived from experimental TOF and laboratory angular distributions, is very similar to results from direct dynamics calculations that used DFT (B3LYP/6-31G**, red dashed curves in Figures 3−5) or the MSINDO semiemperical Hamiltonian (green dash−dot−dashed curves in Figures 3−5) for E_{coll} = 90 kcal mol^{-1}. In order to provide a better fit to the experimental data, we discarded trajectories that produced the CH_3CH_3 molecules with energies less than the ZPE when obtaining the theoretical c.m. translational energy and angular distributions. These trajectories amount to ~30 and ~9% of the inelastic trajectories integrated on the respective MSINDO and B3LYP surfaces. The experimental and calculated c.m. angular distributions (Figure 4) resemble each other; however, the ratio between the forward and sideways scattering intensity is lower in the calculations than that in the experimental data. In general, the experimental and theoretical translational energy and angular distributions indicate strong forward scattering of the oxygen atoms, with very little energy transferred to the ethane collision partner. One final observation of the inelastic scattering channel is that at laboratory angles above 40°, the fits to the TOF distributions in Figure 3 seem increasingly faster than the data. This trend will be discussed in more detail in section V.A.

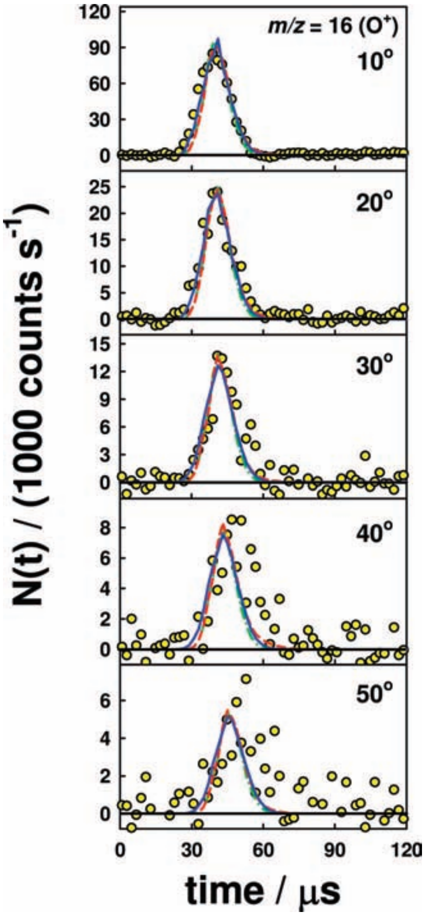

Figure 3. Representative time-of-flight distributions of inelastically scattered oxygen atoms (detected at m/z = 16, O^+) following collisions with ethane at E_{coll} = 90 kcal mol^{-1}. The yellow circles are the experimental data. Laboratory angles at which the data were collected are indicated in each panel. The solid blue curves are the experimental "best-fit" forward-convolution simulations of the data derived from the solid blue curves in the c.m. translational energy and angular distributions shown in Figure 5. The green dash−dot−dashed curves are forward-convolution simulations derived from the MSINDO results shown as green dash−dot−dashed lines in Figure 5. The red dashed curves are forward-convolution simulations derived from the B3LYP results shown as red dashed curves in Figure 5.

While the forward-convolution method produces c.m. translational energy and angular distributions that predict data in Figures 3 and 4 well, it must be noted that due to the fairly low resolution of the data, the forward-convolution fits are not entirely unique. Small changes in the c.m. translational energy and angular distributions will still result in acceptable fits to the data. On the other hand, large changes altering the character of the generated c.m. distributions do not predict acceptable fits to the experimental data. The insensitivity of the experimental data to small changes in the c.m. distributions is the result of high product velocities and, especially, the temporal width of the incident oxygen-atom beam distribution, which inhibits velocity resolution and thus the accuracy of the derived c.m. distributions. Although the velocity resolution is lower than would be desired, general statements about the scattering direction and energy transfer in the c.m. frame can be made with certainty.

B. H-atom Abstraction. Representative TOF distributions collected at five laboratory angles for m/z = 17 (OH^+) are shown as yellow circles in Figure 6, and the corresponding laboratory angular distribution is shown as black solid circles in Figure 7. The blue curves in both Figures 6 and 7 represent the "best-fit"

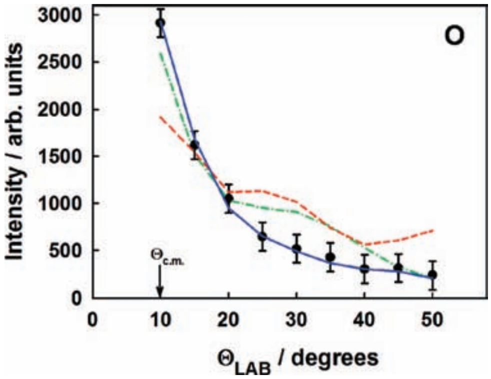

Figure 4. Laboratory angular distribution of inelastically scattered oxygen atoms (detected at m/z = 16, O^+) following collisions with ethane at E_{coll} = 90 kcal mol^{-1}. The black solid circles are the experimental data, and the solid blue line is the experimental "best-fit" forward-convolution simulation of the data derived from the solid blue curves in the c.m. translational energy and angular distributions shown in Figure 5. The green dash−dot−dashed curve is the forward-convolution simulation derived from the MSINDO results shown as green dash−dot−dashed lines in Figure 5. The red dashed curve is the forward-convolution simulation derived from the B3LYP results shown as red dashed curves in Figure 5.

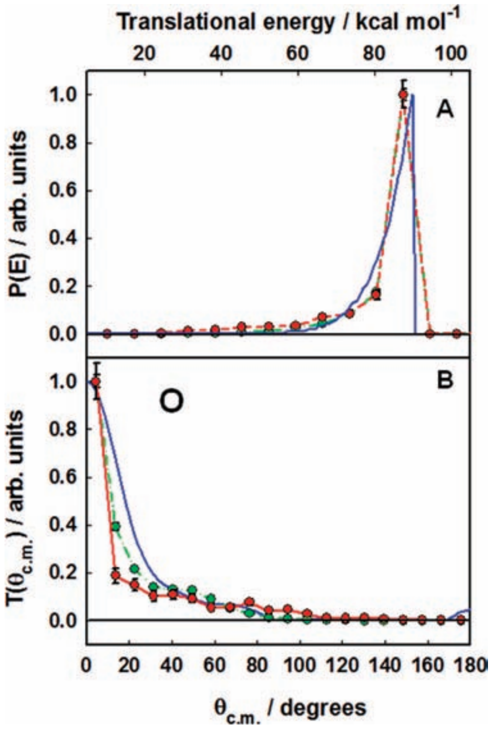

Figure 5. Center-of-mass translational energy (A) and angular (B) distributions for the inelastic scattering of oxygen atoms from ethane, used in the forward-convolution fits of the laboratory time-of-flight and angular distributions for m/z = 16 (Figures 3 and 4). The angular distribution pertains to O atoms. The solid blue curves show the "best-fit" distribution derived through fitting the time-of-flight and laboratory angular distributions via the forward-convolution method. The green circles connected with the green dash−dot−dashed lines represent the distributions obtained from MSINDO calculations at E_{coll} = 90 kcal mol^{-1}. The red circles connected with the red dashed lines represent the distributions obtained from B3LYP calculations at E_{coll} = 90 kcal mol^{-1}. Note that the small bump in Figure 5B rising at 170° is an artifact from the forward-convolution fitting process.

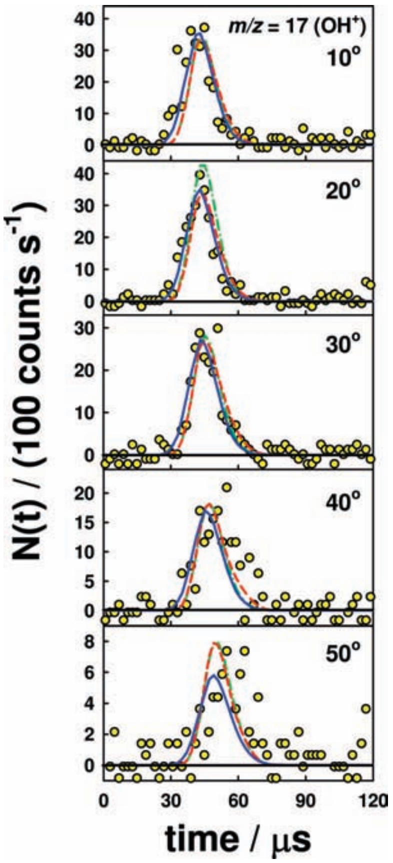

Figure 6. Representative time-of-flight distributions of reactively scattered OH (detected at m/z = 17, OH^+) following the H-atom abstraction reaction of O(^3P) with ethane at E_{coll} = 90 kcal mol^{-1} to produce OH + C_2H_5. The yellow circles are the experimental data. Laboratory angles at which the data were collected are indicated in each panel. The solid blue curves are the experimental "best-fit" forward-convolution simulations of the data derived from the solid blue curves in the c.m. translational energy and angular distributions shown in Figure 8. The green dash−dot−dashed curves are forward-convolution simulations derived from the MSINDO results shown as green dash−dot−dashed lines in Figure 8. The red dashed curves are forward-convolution simulations derived from the B3LYP results shown as red dashed curves in Figure 8.

forward-convolution results using the c.m. translational energy and angular distributions shown as blue curves in Figure 8, respectively. The analysis of the data was based on the assumption that the OH product was the result of the reaction $O(^3P) + CH_3CH_3 \rightarrow OH + CH_3CH_2$. The green dash−dot−dashed curves in Figures 6−8 represent the MSINDO results for this reaction, and higher-level B3LYP results are shown as red dashed curves. The experimental laboratory angular distribution in Figure 7 is reproduced better by the B3LYP prediction than the MSINDO prediction, which reflects the better agreement between the experimental and B3LYP results in the c.m. distributions in Figure 8. The experimental translational energy distribution (Figure 8A) follows the B3LYP distribution fairly well, but it is not as broad as the latter in the lower translational energy range. The MSINDO translational energy distribution has a peak that is slightly lower than the experimental results and is much broader than the experimentally derived distribution. Despite the jagged character of the B3LYP angular distribution (Figure 8B), which results from the relatively small number of reactive trajectories on this surface, the overall trend agrees well with the experimentally derived angular distribution, which has a maximum in the vicinity of the experimental result of 23°. The MSINDO distribution, though predominantly forward-scattered, reaches a maximum at 40° and diminishes more rapidly at sideways/backward angles than either the experimental or the B3LYP distribution. The general agreement between experiment and theory reveals the overall picture of the

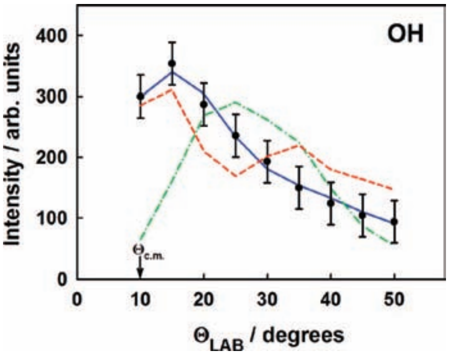

Figure 7. Laboratory angular distribution of the OH product (detected at m/z = 17, OH^+) following the H-atom abstraction reaction of $O(^3P)$ with ethane at E_{coll} = 90 kcal mol^{-1} to produce OH + C_2H_5. The black solid circles are the experimental data, and the solid blue line is the experimental "best-fit" forward-convolution simulation of the data derived from the solid blue curves in the c.m. translational energy and angular distributions shown in Figure 8. The green dash−dot−dashed curve is the forward-convolution simulation derived from the MSINDO results shown as green dash−dot−dashed lines in Figure 8. The red dashed curve is the forward-convolution simulation derived from the B3LYP results shown as red dashed curves in Figure 8.

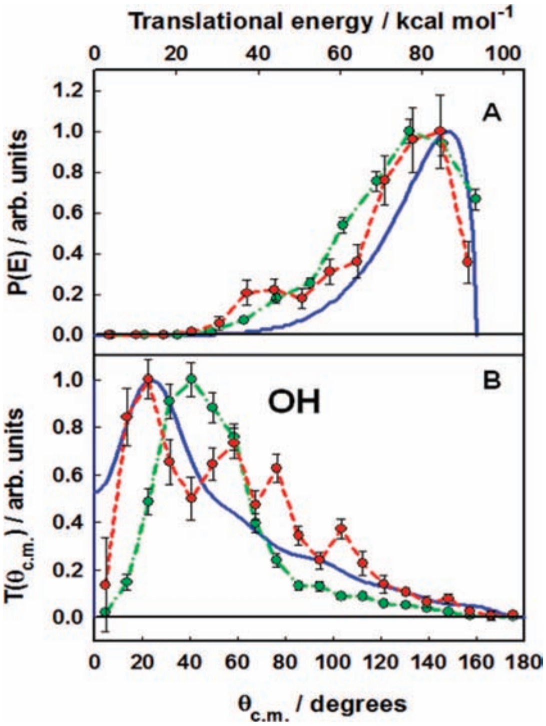

Figure 8. Center-of-mass translational energy (A) and angular (B) distributions for the H-atom abstraction reaction of $O(^3P)$ with ethane at E_{coll} = 90 kcal mol^{-1} to produce OH + C_2H_5, used in the forward-convolution fits of the laboratory time-of-flight and angular distributions for m/z = 17 (Figures 6 and 7). The angular distribution pertains to the OH product. The solid blue curves show the "best-fit" distribution derived through fitting the time-of-flight and laboratory angular distributions via the forward-convolution method. The green circles connected with the green dash−dot−dashed lines represent the distributions obtained from MSINDO calculations. The red circles connected with the red dashed lines represent the distributions obtained from B3LYP calculations.

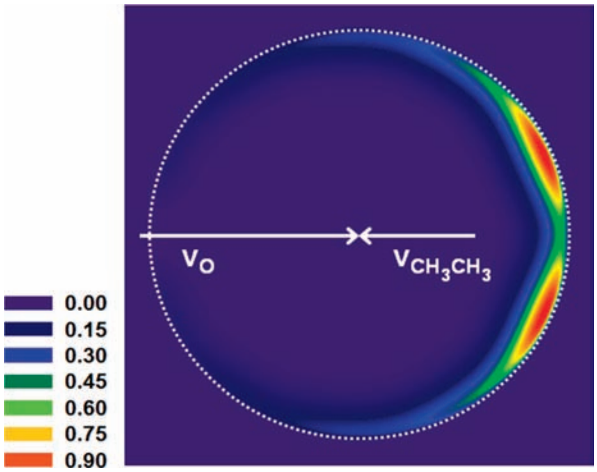

Figure 9. Center-of-mass velocity−flux map of the reactive OH product, derived from the c.m. translational energy and angular distributions shown in Figure 8. The dotted line represents the maximum possible velocity, consistent with conservation of energy and momentum. The red color represents maximum flux.

scattering dynamics for the abstraction reaction; the OH scattering is largely forward, with some intensity extending to sideways angles. Very little translational energy is lost in the collisions, although there is more energy transferred than was observed for the inelastic scattering channel. The c.m. velocity−flux map for OH, created from the experimental c.m. translational energy and angular distributions, is shown in Figure 9.

C. H-Atom Elimination. Figure 10 contains representative TOF distributions, collected for m/z = 43 ($OC_2H_3^+$) and Θ_{LAB} = 7.5−17.5°. The analysis is based on the assumption that the detected product is ethoxy from the $O(^3P) + CH_3CH_3 \rightarrow H + OC_2H_5$ reaction. However, as discussed below, the detected product may be acetaldehyde (CH_3CHO), which results from secondary dissociation of OC_2H_5. The laboratory angular distribution is shown in Figure 11 as black solid circles. Forward-convolution simulated fits to the experimental data are shown in Figures 10 and 11 as blue curves, and the c.m. translational energy and angular distributions underpinning those fits are shown as blue curves in Figure 12. Results from the MSINDO calculations are represented as green dash−dot−dashed curves, and the B3LYP results are represented as red dashed curves in Figures 10−12. Significant differences are apparent when comparing the laboratory angular distributions in Figure 11. Both the MSINDO and B3LYP predictions fail to capture the character of the distribution. The theoretical predictions show a dip in intensity in the laboratory angular distribution at around 12°, just where the experimental distribution reaches a maximum, and the theoretical predictions are much narrower than the experimental distribution. These differences are a manifestation of the differences between the experimental and theoretical c.m. angular distributions (Figure 12B). The c.m. angular distributions, while having some similarities, have quite different shapes. There are three distinct peaks, in the backward, sideways, and forward directions, in the distribution derived from the experimental data. The B3LYP distribution has three peaks in the backward, sideways, and forward directions, but these peaks do not coincide precisely with the experimental peak positions. Particularly, the backward peak by B3LYP appears at around 130−150°, whereas the experimental distribution is low in this range and rises to an apparent maximum at 180°. The MSINDO distribution exhibits only one peak near 110° and is broad in both the forward and backward directions. The experimental and the B3LYP translational energy distributions agree reasonably well (Figure 12A), with maxima near 22 kcal mol^{-1}; however, the MSINDO translational energy distribution is shifted to higher energies. Nevertheless, all three distributions have much lower energies than the available energy (∼81 kcal

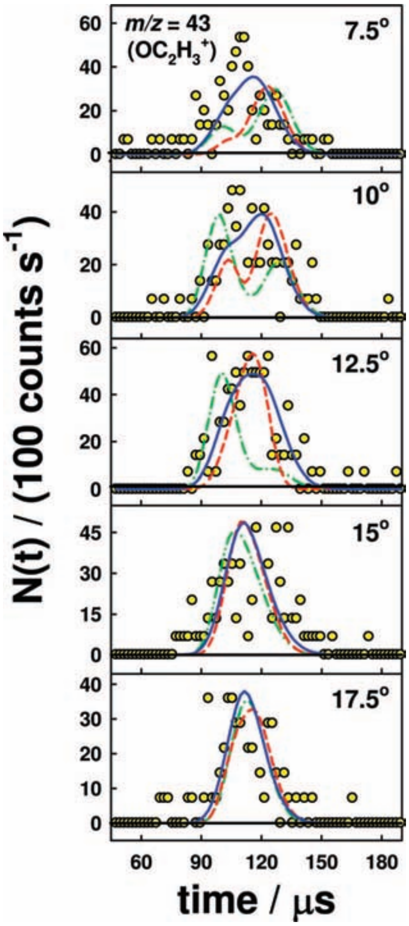

Figure 10. Representative time-of-flight distributions of reactively scattered products detected at $m/z = 43$, $OC_2H_3^+$, following the H-atom elimination reaction of O(^3P) with ethane at $E_{coll} = 90$ kcal mol^{-1} to produce H + OC_2H_5. The yellow circles are the experimental data. Laboratory angles at which the data were collected are indicated in each panel. The solid blue curves are the experimental "best-fit" forward-convolution simulations of the data derived from the solid blue curves in the c.m. translational energy and angular distributions shown in Figure 12. The green dash−dot−dashed curves are forward-convolution simulations derived from the MSINDO results shown as green dash−dot−dashed lines in Figure 12. The red dashed curves are forward-convolution simulations derived from the B3LYP results shown as red dashed curves in Figure 12.

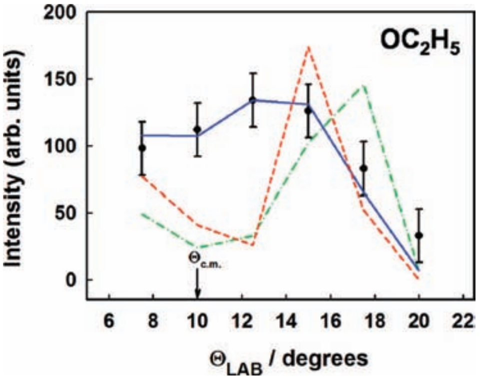

Figure 11. Laboratory angular distribution of the product detected at $m/z = 43$, $OC_2H_3^+$, following the H-atom elimination reaction of O(^3P) with ethane at $E_{coll} = 90$ kcal mol^{-1} to produce H + OC_2H_5. The black solid circles are the experimental data, and the solid blue line is the experimental "best-fit" forward-convolution simulation of the data derived from the solid blue curves in the c.m. translational energy and angular distributions shown in Figure 12. The green dash−dot−dashed curve is the forward-convolution simulation derived from the MSINDO results shown as green dash−dot−dashed lines in Figure 12. The red dashed curve is the forward-convolution simulation derived from the B3LYP results shown as red dashed curves in Figure 12.

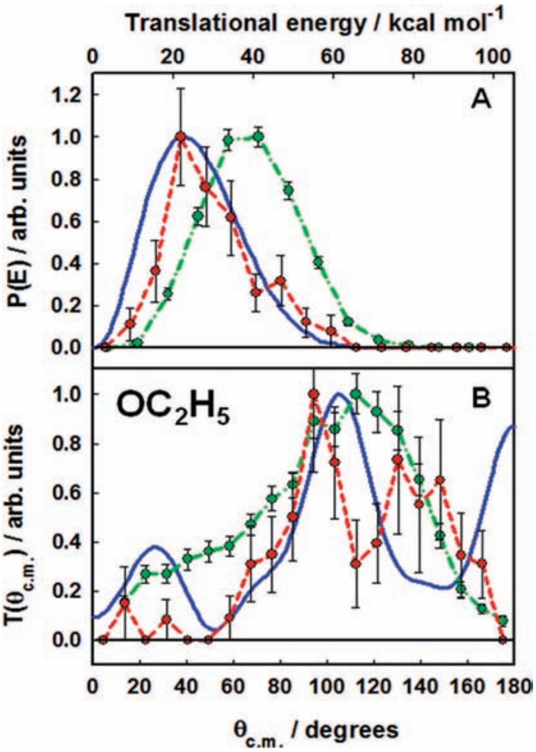

Figure 12. Center-of-mass translational energy (A) and angular (B) distributions for the H-atom elimination reaction of O(^3P) with ethane at $E_{coll} = 90$ kcal mol^{-1} to produce H + OC_2H_5, used in the forward-convolution fit of the laboratory time-of-flight and angular distributions for $m/z = 43$ (Figures 10 and 11). The angular distribution pertains to the product detected at $m/z = 43$ ($OC_2H_3^+$). The solid blue curves show the "best-fit" distribution derived through fitting the time-of-flight and laboratory angular distributions via the forward-convolution method. The green circles connected with the green dash−dot−dashed lines represent the distributions obtained from MSINDO calculations. The red circles connected with the red dashed lines represent the distributions obtained from B3LYP calculations.

mol^{-1}), indicating a large amount of energy transfer from translation to the internal modes of the ethoxy radical.

The range of internal energies of OC_2H_5 suggested by the experimental and B3LYP translational energy distributions is roughly 20−80 kcal mol^{-1}. This entire range is above the barriers for dissociation of the ethoxy radical into $H_2CO + CH_3$ or CH_3CHO + H. Therefore, the product detected at $m/z = 43$ is probably CH_3CHO, which is produced by secondary dissociation of the primary OC_2H_5 product. The implications of secondary dissociation on the experimentally derived dynamics are discussed in section V.C.

It should be noted that the experimentally derived c.m. distributions have significant uncertainty and are mainly useful to show what trends in the c.m. distributions will lead to acceptable fits to the experimental TOF and laboratory angular distributions. It is particularly difficult to obtain experimental c.m. quantities for this channel because limited angular and translational information can be extracted from the data when the entire range of ethoxy c.m. product velocities spans just ~20° in the laboratory frame and the c.m. recoil velocities cover a range that is comparable to the range of O-atom velocities in the incident beam. Nonetheless, an attempt was made to provide the c.m. translational energy and angular distributions that gave the best predictions of the laboratory TOF and angular distributions. The combination of theoretical and experimental results reveals a picture of scattering for the O(^3P) + $CH_3CH_3 \rightarrow H +$ OC_2H_5 reaction wherein the ethoxy product is largely sideways- and backward-scattered, with a relatively small fraction of the available energy released in translation.

D. Attempt to Identify the C−C Bond-Breakage Channel. The theoretical calculations predict that C−C bond breakage may occur, albeit with relatively low probability. The identification of this reaction pathway in the experiment proved to be problematic, and only an upper limit of the relative yield could be determined. Identification of C−C bond breakage may, in principle, be accomplished by detection of either the OCH_3 or the CH_3 product. Unfortunately, both products must be detected at mass-to-charge ratios at which other products can also be detected. Therefore, it is necessary to account for all contributions to the signal at a relevant mass-to-charge ratio in order to determine whether or not C−C bond breakage occurs. Detection of CH_3^+ from the CH_3 product is especially difficult because there is a high background in the detector from dissociative ionization of the CH_3CH_3 reagent. Furthermore, the CH_3 product scatters at higher c.m. velocities than OCH_3 and therefore would have less flux into the detector at a given laboratory angle. Hence, we chose to focus on detection of the OCH_3 product. The parent ion, OCH_3^+, gives a weak signal, and the OCH_3 product is best detected at $m/z = 29$ (HCO^+) or 30 (H_2CO^+), where the signals are largest.[9,30] Although it might also be possible to detect OCH_3 at $m/z = 28$ (CO^+), the signal at this mass-to-charge ratio is relatively low, and the background in the detector is high. Furthermore, another product, C_2H_4, from a possible minor reaction leading to $H_2O + C_2H_4$ (see Table 2), might also be detected at $m/z = 28$. Perhaps the most important problem in the detection of OCH_3 from C−C bond breakage is the likelihood that internally excited OC_2H_5 products dissociate to H_2CO and CH_3. Because the parent OCH_3^+ signal is too weak to detect, the only choice was to try to identify OCH_3 as a component of TOF distributions collected at $m/z =$ 29 or 30, where the secondary H_2CO product could also be detected. Although we studied TOF distributions collected at both $m/z = 29$ and 30, we chose to focus on the TOF distributions collected at $m/z = 29$ for a detailed investigation of the possible $OCH_3 + CH_3$ product channel because TOF distributions collected at $m/z = 29$ gave the better signal-to-noise ratio.

The explanation of the TOF and angular distributions collected at $m/z = 27$ ($C_2H_3^+$) provides a basis for identifying an oxygen-containing product from the data collected at $m/z =$ 29 ($C_2H_5^+$, HCO^+). The four channels expected to contribute signal to the TOF distributions at $m/z = 27$ are inelastic scattering of CH_3CH_3 from O, inelastic scattering of CH_3CH_3 from O_2, C_2H_5 radical formation in the reaction O(^3P) + $CH_3CH_3 \rightarrow OH + C_2H_5$, and ethoxy radical formation (or acetaldehyde formation from secondary dissociation) in the reaction of O(^3P) + $CH_3CH_3 \rightarrow H + OC_2H_5$. Representative TOF distributions for $m/z = 27$ from 10 to 50° are shown as yellow circles in Figure 13. The laboratory angular distribution is shown as black solid circles in Figure 14. The curves in Figure 13 represent the forward-convolution fits to the laboratory TOF data, obtained from considering all channels that contribute to the overall signal. The c.m. translational energy and angular distributions that lead to these fits and to the fit of the laboratory angular distribution in Figure 14 are shown in Figure 15.

The solid and dashed red curves in Figure 15 come from fitting the inelastic scattering of ethane from O atoms. The solid red curves in Figure 15 are broadened (both in angle and energy) versions of the experimentally derived translational energy and angular distributions shown for O-atom inelastic scattering in Figure 5. Broadening of the distributions was required to provide reasonable forward-convolution fits to the $m/z = 27$ TOF distributions. A second set of translational energy and angular distributions (dashed red curves in Figure 15) was also needed in fitting the inelastic scattering signal from CH_3CH_3. This second set of c.m. distributions was necessary because of the assumption in the forward-convolution method that only one set of uncoupled c.m. translational energy and angular distributions is necessary for each channel. If, however, there is coupling between the translational energy and angular distribution, manifested in the variation of the c.m. translational energy distribution with the c.m. angle, more than one set of c.m. distributions must be included to provide a fit to the experimental data.[31] On the basis of the slowing of the inelastic scattering signal observed at $m/z = 16$ for laboratory angles greater than 40°, there appears to be coupling between the translational energy and angular distributions for the O-atom inelastic

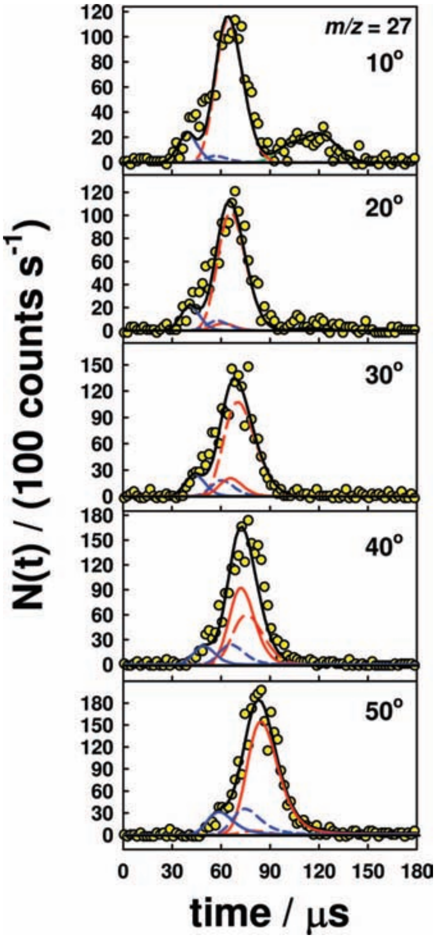

Figure 13. Representative time-of-flight distributions collected at m/z = 27 ($C_2H_3^+$) following O(^3P) collisions with ethane at $E_{coll} = 90$ kcal mol^{-1} and O_2 collisions with ethane at $E_{coll} = 135$ kcal mol^{-1}. The yellow circles are the experimental data. Laboratory angles at which the data were collected are indicated in each panel. Four possible channels give rise to signal at $m/z = 27$ as a result of product fragmentation in the ionizer, inelastic scattering of ethane from O_2 (blue solid) and O (red solid and red dashed), H-atom abstraction to form OH and C_2H_5 (blue dashed), and H-atom elimination to form OC_2H_5 (or CH_3CHO + H) and H (green dash−dot−dashed, ∼110 µs). The contribution of each channel is derived from c.m. translational energy and angular distributions of the corresponding color/texture in Figure 15. The sum of the contributions of all of the channels in each panel is shown as a solid black curve.

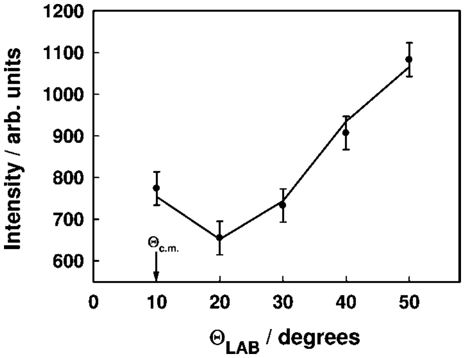

Figure 14. Laboratory angular distribution for all products yielding signal at $m/z = 27$ ($C_2H_3^+$) following O(^3P) collisions with ethane at $E_{coll} = 90$ kcal mol^{-1} and O_2 collisions with ethane at $E_{coll} = 135$ kcal mol^{-1}. The black solid circles are the experimental data. The solid black curve is the forward-convolution fit to the data, derived from the sum of all channels delineated in the c.m. translational energy and angular distributions in Figure 15.

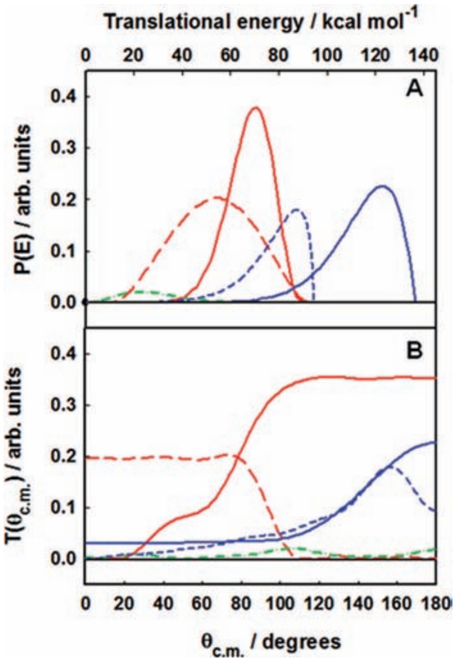

Figure 15. Center-of-mass translational energy (A) and angular (B) distributions for all of the channels that give rise to the signal observed at $m/z = 27$ ($C_2H_3^+$), inelastic scattering of ethane from O_2 (blue solid) and O (red solid and red dashed), H-atom abstraction to form OH and C_2H_5 (blue dashed), and H-atom elimination to form OC_2H_5 or CH_3CHO + H (green dash−dot−dashed). Each channel is normalized to illustrate its relative weight used in the forward-convolution fit to the laboratory TOF and angular distributions (Figures 13 and 14).

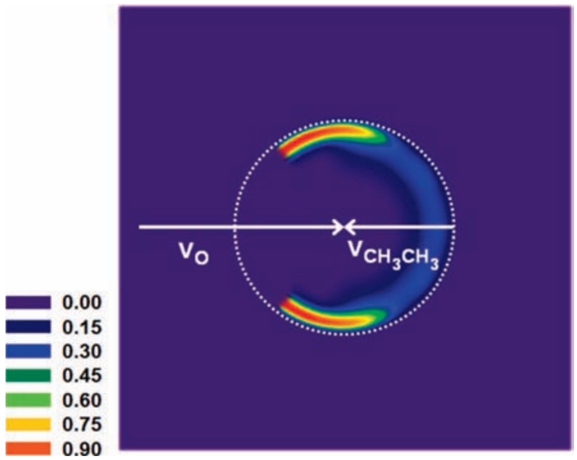

Figure 16. Center-of-mass velocity−flux map of inelastically scattered CH_3CH_3, following collisions with O(^3P) at $E_{coll} = 90$ kcal mol^{-1}, derived from the c.m. translational energy and angular distributions shown as red curves in Figure 15. The dotted line represents the maximum possible velocity, consistent with conservation of energy and momentum. Only the c.m. angles for which the experiment was sensitive are shown. The red color represents maximum flux. Note that this plot is only for scattered CH_3CH_3, and the color scheme merely represents normalization to the maximum relative flux of CH_3CH_3. CH_3CH_3 products scattered from high-impact-parameter collisions are not represented in this figure, as their flux would be off scale.

scattering channel. For the laboratory angular range of this experiment (see Figure 2), the O-atom inelastic scattering signal that can be measured comes from events in which the O atoms scatter mostly forward (glancing collisions) and, to a much lesser extent, sideways in the c.m. frame. Forward-scattered O atoms are detected at c.m. angles near 0°, which is the direction of the reagent O-atoms. CH_3CH_3 scatters in the opposite direction of the O atoms in the c.m. frame; therefore, these experiments are sensitive to CH_3CH_3 molecules that scatter backward or sideways from their point of view (low-impact-parameter collisions). Because we define the c.m. angle with respect to the direction of the reagent O atoms, we refer to such CH_3CH_3 molecules as "forward-scattered." As the inelastic products that scatter into the forward direction are probed preferentially, the detection of O provides information on high-impact-parameter ("glancing") collisions, whereas the detection of CH_3CH_3 provides information on low-impact-parameter ("head-on") collisions. Collisions with impact parameters in between will lead to sideways scattering, and detection of either product at large laboratory angles may provide information on these collisions. The observation of a slowing of the inelastically scattered O atoms relative to the predicted flight times at larger laboratory angles (Figure 3) suggests that the c.m. translational energy and angular distributions in Figure 5 do not perfectly predict the dynamics of lower-impact-parameter collisions that lead to scattering at the larger angles. The coupling of the translational energy and angular distributions that is implied by this result is accentuated when deriving c.m translational energy and angular distributions from the CH_3CH_3 TOF distributions because the slower recoil velocities of CH_3CH_3 result in the sampling of a wider range of c.m. angles for a given range of laboratory angles. Therefore, in order to fit the inelastic component of the $m/z = 27$ TOF distributions, it was necessary to simulate this coupling by using two sets of c.m. translational energy and angular distributions in the fits (red curves in Figures 13 and 15). These distributions reflect lower translational energies for lower-impact-parameter collisions that scatter ethane into the "forward" direction in our experiment. Reduced translational energies for lower-impact-parameter collisions were also observed in the B3LYP and MSINDO calculations on the inelastic scattering of O from ethane, adding validity to the conclusion that coupling of the c.m. translational energy and angular distributions must be taken into account in the fitting of the inelastically scattered ethane. A c.m. velocity−flux map showing ethane scattering inelastically from O(^3P) in the sideways and backward directions (from the ethane point of view) is shown in Figure 16. Only the laboratory angular range within which data were collected is shown; thus, the high-impact parameter component, which would be off scale, is not presented in this figure.

CH_3CH_3 may also scatter inelastically from O_2 molecules in the beam. In order to include this contribution to the $m/z = 27$

signal, translational energy and angular distributions derived from an experiment in which Ar was scattered from ethane at E_{coll} = 115 kcal mol^{-1} were used,[32] and it was assumed that the dynamics for ethane scattering from O_2 are similar to those for ethane scattering from Ar. The average collision energy between O_2 and ethane in these experiments is 135 kcal mol^{-1}, which is 20 kcal mol^{-1} higher than that in the Ar scattering experiment; therefore, the translational energy distribution obtained from the Ar + ethane experiment was shifted by 20 kcal mol^{-1} to higher energies while preserving its shape. The contribution of ethane inelastic scattering from O_2 is shown as the solid blue curves in Figures 13 and 15.

The ethyl radical product (C_2H_5) from the H-atom abstraction reaction also contributes signal to the m/z = 27 data. The contribution of this signal was calculated with the experimentally derived translational energy and angular distributions in Figure 8, where the angular distribution was reversed (180° − θ) to correspond to the C_2H_5 product rather than OH. The contribution of the H-atom abstraction channel is shown as dashed blue curves in Figures 13 and 15.

The final channel considered in the m/z = 27 data was the ethoxy (or acetaldehyde) product, OC_2H_5 (or CH_3CHO), from the H-atom elimination reaction. This channel was included by using the c.m. translational energy and angular distributions obtained from analyzing the signals at m/z = 43 (Figure 12). Contributions from the assumed H-atom elimination reaction are shown as green dash−dot−dashed curves in Figures 13 and 15.

The black curves in Figure 13 show the predicted TOF distributions resulting from taking weighted contributions of all four channels into account in the forward convolution, and the black curve in Figure 14 shows the predicted laboratory angular distribution. Inclusion of all four channels was necessary to produce good fits for both the experimental TOF and angular distributions. Relative channel weights were adjusted to provide the best fit to the experimental data, and all distributions in Figure 15 have been normalized to reflect their relative channel weight. As can be seen, inelastic scattering of CH_3CH_3 from O atoms accounts for the bulk of the signal detected at m/z = 27. Inelastic scattering of CH_3CH_3 from O_2 is responsible for the relatively small and fast signal at short arrival times. (Note that the coupling between translational energy and angle was not considered for this channel because the signal was not large enough nor of sufficient quality to justify such a detailed analysis.) Of the remaining two channels, H-atom abstraction contributed significantly, and the H-atom elimination channel contributed negligibly.

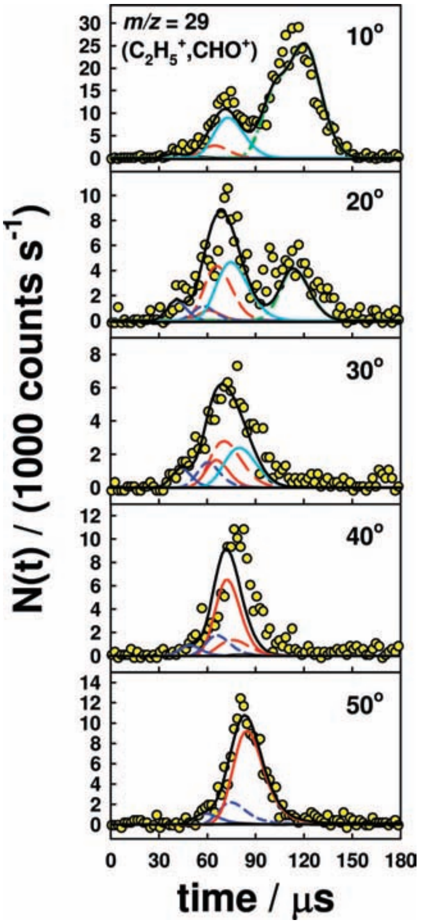

Figure 17. Representative time-of-flight distributions collected at m/z = 29 ($C_2H_5^+$, CHO^+) following O(^3P) collisions with ethane at E_{coll} = 90 kcal mol^{-1} and O_2 collisions with ethane at E_{coll} = 135 kcal mol^{-1}. The yellow circles are the experimental data. Laboratory angles at which the data were collected are indicated in each panel. Five possible channels give rise to signal at m/z = 29 as a result of product fragmentation in the ionizer, inelastic scattering of ethane from O_2 (blue solid) and O (red solid and red dashed), H-atom abstraction to form OH and C_2H_5 (blue dashed), H-atom elimination to form OC_2H_5 (or CH_3CHO + H) and H (green dash−dot−dashed, ~110 μs), and another process that probably produces OCH_3, CH_2OH, and/or H_2CO (cyan). The contribution of each channel is derived from c.m. translational energy and angular distributions of corresponding color/texture in Figure 19. The sum of the contributions of all of the channels in each panel is shown as a solid black curve.

The TOF distributions at m/z = 29 contain signals from all of the channels identified as contributors to the m/z = 27 distribution, and the m/z = 29 signal might also contain additional signal, for example, from C−C bond breakage to produce OCH_3 + CH_3 or secondary dissociation of primary OC_2H_5 into H_2CO + CH_3. H_2CO or CH_2OH from secondary dissociation or isomerization, respectively, of the primary OCH_3 product might also contribute signal at m/z = 29. Representative TOF distributions collected at m/z = 29 are shown as yellow circles in Figure 17. The laboratory angular distribution is shown as black solid circles in Figure 18. Figure 19 contains the c.m. translational energy and angular distributions for the two O-atom inelastic scattering channels (red solid and dashed curves), O_2 inelastic scattering channel (blue solid curves), H-atom abstraction channel (blue dashed curves), and ethoxy (or acetaldehyde) product (green dash−dot−dashed curves). These channels alone were grossly insufficient to provide good fits to the laboratory TOF and angular distributions. A fifth channel was thus added, represented by the cyan curves in Figures 17 and 19. For the purposes of this analysis, this channel was assumed to come from the primary OCH_3 product of the reaction, O(^3P) + $CH_3CH_3 \rightarrow OCH_3 + CH_3$. The "fifth channel" could not be the result of ethoxy or acetaldehyde cracking to m/z = 29 in the ionizer because these products scatter with low velocities in the c.m. frame and can thus be easily associated with the slowest peak in the m/z = 29 TOF distributions collected at small laboratory angles (arrival times near 120 μs in the TOF distributions seen in the top two panels in Figure 17). The necessity to account for another oxygen-containing product in the fits to the m/z = 29 data is evidence for primary C−C bond breakage and/or secondary dissociation of primary OC_2H_5. Assuming that all of the signal is the result of primary C−C bond breakage, the experimental translational energy distribution for this channel has a maximum at ~30 kcal mol^{-1} and indicates that a relatively small fraction of the available energy (~91 kcal mol^{-1}) goes into translational energy in the products. The c.m.

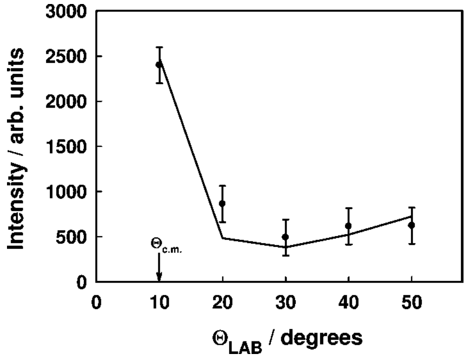

Figure 18. Laboratory angular distribution for all products yielding signal at m/z = 29 ($C_2H_5^+$, CHO^+) following O(^3P) collisions with ethane at E_{coll} = 90 kcal mol^{-1} and O_2 collisions with ethane at E_{coll} = 135 kcal mol^{-1}. The black solid circles are the experimental data. The solid black curve is the forward-convolution fit to the data, derived from the sum of all channels delineated in the c.m. translational energy and angular distributions in Figure 19.

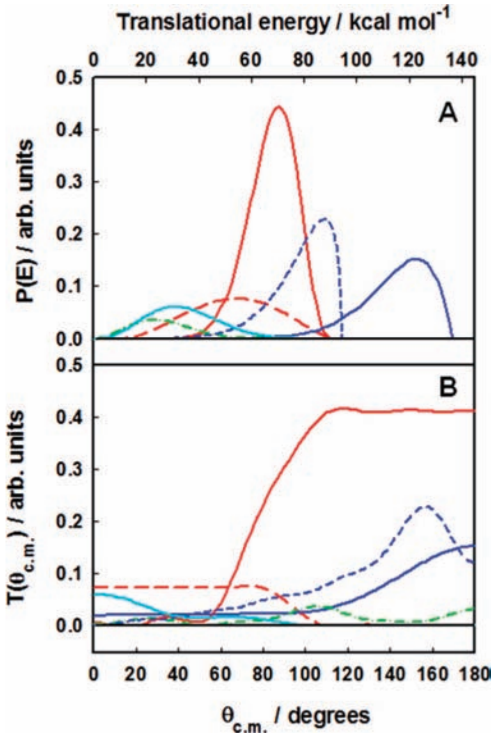

Figure 19. Center-of-mass translational energy (A) and angular (B) distributions for all of the channels that give rise to the signal observed at m/z = 29 ($C_2H_5^+$, CHO^+), inelastic scattering of ethane from O_2 (blue solid) and O (red solid and red dashed), H-atom abstraction to form OH and C_2H_5 (blue dashed), H-atom elimination to form OC_2H_5 or CH_3CHO + H (green dash−dot−dashed), and another process that probably produces OCH_3, CH_2OH, and/or H_2CO (cyan). Each channel is normalized to illustrate its relative weight used in the forward-convolution fit to the laboratory TOF and angular distributions (Figures 17 and 18).

angular distribution indicates that the OCH_3 product is largely forward scattered, with some intensity in the sideways direction. It should be noted, however, that the uncertainty of these c.m. distributions is high because they were derived from TOF and angular distributions with many overlapping components. More importantly, the c.m. quantities were derived under an assumption that is likely not to be valid.

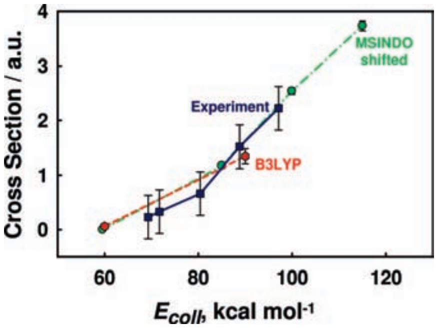

Figure 20. Experimental and calculated excitation functions (cross section versus collision energy) for the O(^3P) + C_2H_6 → C_2H_5O + H reaction. Experimental data collected at m/z = 43 ($C_2H_3O^+$) are shown as blue squares connected with a solid blue line. The green circles connected with a green dash−dot−dashed line are the MSINDO calculated cross sections shifted to higher energy by 25 kcal mol^{-1}. The B3LYP calculated cross sections are shown as the red hexagons connected with the red dashed line.

E. Excitation Function for O(^{3}*P*) + C_2H_6 → C_2H_5O + H. The low product recoil velocities for the ethoxy (or acetaldehyde) product, which concentrate the flux over a narrow range of laboratory angles, make it possible to obtain a relative excitation function for the H-atom elimination reaction, as has been done earlier for other reactions.[9,21,33] Representative TOF distributions for the product detected at m/z = 43 were collected for five c.m. collision energies, E_{coll} = 69, 72, 80.4, 89, and 97 kcal mol^{-1}. For data collection at each collision energy, the laboratory angle was adjusted slightly so that it coincided with the direction of the c.m. velocity. Thus, the laboratory angle varied from 9.5 to 11.5°. The signal intensities of the scattered products varied with the c.m. collision energy in part because the corresponding oxygen-atom flux in the hyperthermal beam varied. In order to obtain the dependence of the scattered flux on collision energy alone, the integrated fluxes derived from the m/z = 43 TOF distributions were divided by the corresponding relative integrated intensity of the oxygen-atom beam. The relative "ethoxy" product fluxes, corrected for the incident oxygen-atom beam intensity, are shown as blue squares in Figure 20. Also shown in Figure 20 are the MSINDO (green circles) and B3LYP (purple hexagons) calculated excitation functions. For this experiment, it would be ideal to reach low enough collision energies to observe the reaction threshold. We were, however, unable to produce a slow enough O-atom beam to reach collision energies below 69 kcal mol^{-1}. As signal that must have originated from an ethoxy product was observed at this collision energy, all data for this product were collected with c.m collision energies that were above the reaction threshold. In order to match the experimental and B3LYP excitation functions, the calculated MSINDO excitation function was shifted to higher energy by 25 kcal mol^{-1}. Within experimental error, the shapes of both theoretical curves match the shape of the experimental excitation function. Although initially above the experimental curve (thus reflecting a barrier that is too low), the B3LYP curve increases more slowly and eventually falls below the experimental curve at higher collision energies. On the basis of an earlier study of the O + CH_4 reaction,[9] this underestimation at high energies could reflect excited-state contributions that are not included in the calculation. A simple extrapolation of the experimental excitation function suggests that the barrier for the O(^3P) + CH_3CH_3 → H + OC_2H_5 reaction might be somewhat less than 60 kcal mol^{-1}. This should be considered an upper limit, however, since the experiment was unable to probe the exact position of the barrier. Note that the apparent threshold estimate from B3LYP is only slightly below this experimental estimate, while the MSINDO threshold is significantly lower (at roughly 35 kcal/mol). Thus, the difference between B3LYP and MSINDO threshold energies is quite a bit larger than the difference in barrier heights. This result correlates with more important ZPE violation in the MSINDO calculation (noted earlier).

Previous work on $O(^3P) + CH_4$ strongly suggests that the ground triplet surface and the first excited triplet surface play a role in the dynamics of $O(^3P)$ + alkane reactions at hyperthermal energies.[9] In order to reproduce the steeply rising experimental excitation function for the $O(^3P) + CH_4 \rightarrow H + OCH_3$ reaction, contributions from both the 1 ^3A and 2 ^3A surfaces had to be included. In the present study, all of the QCT trajectories were integrated only on the ground triplet surface; therefore, the analogous excitation function estimate cannot be made. But we can speculate that the reactive cross sections will rise more steeply when the excited-state reaction is added to the ground-state result. We thus expect the theoretical cross sections to match the shape of the experimental excitation function better when excited-state contributions are included.

F. Relative Product Yields. To determine the relative product yields, the relative signal for each channel was measured, under the assumptions that the $m/z = 43$ signal came from the $OC_2H_5 + H$ product channel and the "fifth" component of the $m/z = 29$ signal came from the $OCH_3 + CH_3$ product channel. This was done by choosing one product for each channel (O for inelastic scattering, OH for H-atom abstraction, "OC_2H_5" for H-atom elimination, and "OCH_3" for C−C bond breakage) and determining all possible ionizer fragments for that product that could contribute to the overall signal. TOF distributions were collected at a laboratory angle of 10° for all possible ionizer fragments of the products. For the inelastic scattering and H-atom abstraction channels, all of the signals used in calculating the relative product yields were obtained from TOF distributions at $m/z = 16$ and 17, respectively (i.e., there were no significant ionizer fragments to consider). For the assumed H-atom elimination and C−C bond-breakage channels, however, several fragments would be produced when the product entered the ionizer, resulting in a reduced signal at $m/z = 43$ for the H-atom elimination channel and at $m/z = 29$ for the C−C bond-breakage channel. The percentage of these channels resulting in signal at $m/z = 43$ for OC_2H_5 and at $m/z = 29$ for OCH_3 was determined. For example, the signal at $m/z = 43$ was determined to be 16% of the overall signal detected at all ionizer fragments of the ethoxy radical. For OCH_3, the fraction of the signal detected at $m/z = 29$ was estimated based on the known cracking pattern of OCH_3.[30] Integrated cross sections for each channel were obtained from the forward-convolution fitting of the TOF distributions of the various products and were corrected for the percentage contribution of the measured product fragment to the overall signal for the relevant product. The integrated cross sections were also corrected for the total ionization cross sections of each product species. The resulting experimental relative product yields at $E_{\mathrm{coll}} = 90$ kcal mol^{-1} for all observed channels are included in Table 2. Given the assumptions in this analysis, the relative yield for C−C bond breakage must be considered to be an upper limit, and it could be as low as zero. In addition, the relative yield for H-atom elimination is a lower limit, as a significant fraction of primary OC_2H_5 may dissociate to $H_2CO + CH_3$. Note that we were unable to observe evidence for the $O(^3P) + CH_3CH_3 \rightarrow CH_3CH + H_2O$ reaction in our experiment.

The comparison between the experimental and theoretical branching fractions is somewhat problematic because both experiment and theory have difficulty defining the total cross section. As discussed in section II.B., the total cross section from theory is dependent on the maximum impact parameter used. In the experiment, the accuracies of the integrated cross sections for each channel are dependent, in part, on the accuracies of the c.m. translational energy and angular distributions. Note that the c.m. angular distribution for inelastic scattering to produce O is extrapolated to 0° because it was not possible to observe signal at a laboratory angle corresponding to $\theta = 0°$ because this would require the O-atom beam to be directed into the detector. As most of the inelastically scattered O atoms scatter forward through high-impact-parameter collisions, the extrapolation of the angular distribution to $\theta = 0°$ strongly affects the accuracy of the integral cross section for inelastic scattering. Thus, there is considerable uncertainty in the relative total cross section. Both the experimental and theoretical branching fractions for inelastic scattering happen to come out close to 80% for a collision energy of 90 kcal mol^{-1} (see Table 2). By taking this fortuitous agreement as a fitted result, the arbitrariness of the comparison between the experimental and theoretical branching fractions is removed.

V. Discussion

A. Inelastic Scattering. The oxygen-atom beam contained both O and O_2; consequently, evidence for inelastic collisions between ethane and both O and O_2 was observed in the experiments. Most of the data on inelastic collisions pertains to O atoms and ethane molecules. Inelastically scattered O atoms and ethane molecules were detected in the laboratory angular range of experiments (see Newton diagram in Figure 2). O atoms scattered strongly in the forward direction with very little loss of translational energy, implying a preponderance of large-impact-parameter collisions. These observations were matched well by the results of the theoretical calculations. Although the laboratory TOF and angular distributions for inelastically scattered O atoms (Figures 3 and 4) were predicted fairly well by the c.m. translational energy and angular distributions shown in Figure 5, there is a slight discrepancy between the actual and predicted TOF distributions corresponding to laboratory angles of 40° and above. The inability of a single pair of translational energy and angular distributions to capture the TOF distributions at all laboratory angles indicates a breakdown of the assumption (in the forward-convolution method) that the c.m. translational energy and angular distributions are separable. The data indicate that O atoms that scatter at larger laboratory angles, corresponding to sideways scattering in the c.m frame (see Figure 2), travel at slower velocities than predicted. Scattering at larger c.m. angles is linked with smaller-impact-parameter collisions. Such collisions apparently result in higher energy transfer than collisions with larger impact parameters that lead to forward-scattered O atoms.

The analysis of the inelastically scattered ethane molecules, detected at $m/z = 27$, also revealed the coupling between the c.m. translational energy and angular distributions. In order to fit the TOF distributions collected at $m/z = 27$, which correspond in our experiment to ethane molecules that scatter in the forward and sideways directions with respect to the direction of the reagent O atoms, a translational energy distribution that was broader and had a lower average translational energy than the distribution used to fit the $m/z = 16$ (O^+) TOF data was required. Furthermore, because the coupling between product translation and angle was so strong, the $m/z = 27$ TOF distributions could only be fit with the use of two c.m. translational energy and angular distributions. The use of two sets of distributions in the forward-convolution analysis permits an approximate description of the coupling between product translation and angle.[31]

The analysis indicated that as the ethane molecules become more forward scattered (corresponding to lower-impact-parameter collisions), the energy in translation decreases. This observation suggests that ethane molecules become increasingly internally excited as collisions become more “head on.” In summary, the majority of the oxygen atoms and ethane molecules scatter from each other at large impact parameters with little loss in translational energy; however, some inelastic collisions occur at smaller impact parameters in which the O atom rebounds from ethane in a sideways or backward direction, leading to significant decreases (>20%) in translational energy and a concomitant increase in internal excitation in the ethane molecule. As shown in Supporting Information, Figure SI-8, the theoretical calculations confirm the conclusions of the experiment that the product translational energy and angular distributions are coupled.

The inelastic scattering of ethane molecules from O_2 in the hyperthermal beam was modeled satisfactorily with the use of c.m. translational energy and angular distributions whose shapes were taken from experiments on inelastic scattering of ethane from Ar. The success of the fits is seen in the fast edges of the TOF distributions in Figures 13 and 17. However, the low signals observed for ethane molecules scattering from O_2 in these experiments made it difficult to draw detailed conclusions about the relative similarity of the inelastic scattering of ethane from Ar versus O_2.

B. H-Atom Abstraction. Abstraction of a H atom from ethane by O(^3P) produces OH, which scatters predominantly in the forward direction, with a maximum flux at a c.m. angle of 23° and with relatively little loss of translational energy (see Figure 8). The mass combination of the O(^3P) + $CH_3CH_3 \rightarrow OH + C_2H_5$ reaction may be viewed in terms of a heavy−light−heavy model, where the transferred atom is light and there is a propensity for the system to conserve orbital angular momentum during the reaction. It is thus expected that most of the translational energy stays intact after the collision, which would be especially true for reactions occurring at large impact parameters. Examination of the impact parameter dependence of the energy partitioning reveals that, for large-impact-parameter reactive collisions (average impact parameter = 4.2 a_0), about 92% of the available energy is channeled into translation, 1.6% to OH vibration, 4.1% to OH rotation, and 2.1% to C_2H_5 internal motion. On the other hand, for low-impact-parameter collisions (average impact parameter = 1.8 a_0), the product pair appears with 61.6% of the available energy in translation, 4.6% in OH vibration, 8.6% in OH rotation, and 25.2% in C_2H_5 internal excitation. The above values are averages from the B3LYP trajectories calculated at $E_{\mathrm{coll}} = 90$ kcal mol^{-1}. Examination of the trajectories revealed that large amounts of energy were deposited in the ethyl radical in “head on” collisions (roughly along the line of O−H−C). However, only a small fraction of the reactive collisions involves such low-impact parameters. The OH products from these collisions may scatter sideways and backward, typical of the rebound mechanism that is observed for H-atom abstraction by O(^3P) at low collision energies.[2] The predominant forward scattering of OH and large product translational energies indicate that a stripping reaction is most probable at these hyperthermal collision energies.

The opacity function for H-atom abstraction (Figure SI-3, Supporting Information) supports the picture of the dynamics described above. There is a clear trend for a decrease in reactivity at lower impact parameters and an increase in reactivity at larger impact parameters as the collision energy increases. It is thus expected that the stripping mechanism would dominate over the rebound mechanism in the hyperthermal reactions studied in the current experiment. The decrease in low-impact-parameter reactive events that lead to OH products as the collision energy increases may be explained in part by competition from the H-atom elimination reaction channel, whose cross section rises quickly with collision energy above the threshold of ∼50 kcal/mol (Figure SI-2, Supporting Information).

C. H-Atom Elimination. The dynamical behavior of the product detected at $m/z = 43$ suggests that it is the OC_2H_5 radical from the H-atom elimination reaction. However, if OC_2H_5 is formed with internal excitation above 20 kcal mol^{-1}, then it would undergo secondary dissociation to H and CH_3CHO (acetaldehyde, and perhaps other isomers), and the secondary, not primary, product would be detected at $m/z = 43$. Note that the flight time to the detector is ∼100 μs, and the specific rate coefficients $k(E)$ for unimolecular decomposition to H + CH_3CHO are $>10^{-6}$ for internal energies that exceed the dissociation threshold;[34] therefore, essentially all OC_2H_5 product molecules with internal energies greater than 20 kcal mol^{-1} would dissociate before reaching the detector.

In fact, the theoretical calculations predict that the H-atom elimination reaction will produce OC_2H_5 with more than enough internal energy to dissociate. The B3LYP translational energy distribution for H-atom elimination falls to zero at a maximum energy of ∼60 kcal mol^{-1} (Figure 12). Given an available energy of ∼80 kcal mol^{-1} (Figure 1), the minimum internal energy in OC_2H_5 would be 20 kcal mol^{-1}, which is sufficient to overcome the barrier to dissociation. Because the calculated trajectories were stopped when the c.m. distance between the products exceeded 12 a_0 (MSINDO) or 15 a_0 (B3LYP), the trajectories that were assigned to the OC_2H_5 + H channel were not propagated long enough to observe the expected complete secondary dissociation of OC_2H_5. Nevertheless, with a collision energy of 90 kcal mol^{-1}, OC_2H_5 underwent fast dissociation or isomerization in 12−23% of the trajectories that were assigned to H-atom elimination. On the MSINDO surface, we ran 10000 trajectories (trajs) and obtained the following results for H-atom elimination: OC_2H_5 + H (1000 trajs), CH_3CHO + 2H (200 trajs), $H_2CO + CH_3$ + H (50 trajs), CH_3CHOH + H (42 trajs). On the B3LYP surface, 1000 trajectories were run, and the results were OC_2H_5 + H (69 trajs), CH_3CHO + 2H (3 trajs), $H_2CO + CH_3$ + H (5 trajs), CH_3CHOH + H (1 traj). If the trajectories were propagated longer, all of the primary OC_2H_5 products would likely dissociate.

The branching between the secondary dissociation pathways remains unresolved by theory. On the MSINDO surface, the $OC_2H_5 \rightarrow CH_3CHO$ + H dissociation pathway is preferred. However, on the B3LYP surface, the $OC_2H_5 \rightarrow H_2CO + CH_3$ pathway seems to be preferred, although the statistics are poor. Hase and co-workers[12] studied O(^3P) + CH_3CH_3 reactions theoretically at a higher collision energy of 115 kcal mol^{-1}, and they observed many three-body product channels, with CH_3CHO + 2H being dominant over $H_2CO + CH_3$ + H. Hoyermann et al.[34] have studied the kinetics of decomposition of the ethoxy radical starting with various distributions of internal energy. With lower internal energies, OC_2H_5 dissociates preferentially to $H_2CO + CH_3$, but with higher internal energies, the preference shifts to CH_3CHO + H. These results come from experiments and calculations that reproduce the experiments with a statistical model. In hyperthermal collisions of O(^3P) with CH_3CH_3, our theoretical calculations suggest that a fraction of the nascent OC_2H_5 dissociates before intramolecular vibrational redistribution occurs; thus, the secondary dissociation of OC_2H_5

is likely to be nonstatistical. Perhaps a fraction of the OC_2H_5 product dissociates promptly, and a fraction dissociates statistically. There is insufficient information to draw conclusions about the branching between the secondary dissociation pathways of OC_2H_5, but theoretical calculations and the results of Hoyermann et al. suggest that $CH_3CHO + H$ and $H_2CO + CH_3 + H$ are likely product channels.

The preponderance of the evidence thus leads to the conclusion that the product detected at $m/z = 43$ (also detected as signal at long times at $m/z = 27$, 29, and 30) is likely CH_3CHO that comes from secondary dissociation of the primary OC_2H_5 product. The assumption in the analysis that the product was OC_2H_5 was therefore not entirely valid and may be part of the reason for the discrepancies between the experimental and theoretical angular distributions (Figure 11). If, however, in the secondary dissociation process, CH_3CHO recoils from the H atom at low velocities, then the dynamics of CH_3CHO would mirror those of OC_2H_5. Indeed, the laboratory angular distribution is consistent with low product velocities, as it is diminished above a laboratory angle of 20° (see Figures 2 and 11). The relatively good agreement between the experimental and theoretical translational energy distributions for H-atom elimination (Figure 12A) and the rough agreement between the experimental and theoretical angular distributions of OC_2H_5 (Figure 12B) support the supposition that the experimental analysis captures the essential features of the dynamics of the primary H-atom elimination reaction.

The H-atom elimination reaction is the major competing reactive pathway for H-atom abstraction at relatively small impact parameters. (The opacity functions in Figure SI-4, Supporting Information, confirm the propensity of the reaction to occur at low-impact parameters.) In sharp contrast to the energy disposal scheme found for the abstraction reaction, the majority of the initial relative translational energy is transferred to internal energy of OC_2H_5. On average, 64% of the available energy is channeled into internal excitation of OC_2H_5, based on both the experimental and B3LYP translational energy distributions (Figure 12A). This result is not surprising because the $O(^3P) + CH_3CH_3 \rightarrow C_2H_5O + H$ reaction may be viewed as a heavy−heavy−light reaction, where the departing atom is light. In a reaction of this type, the initial orbital angular momentum tends to be converted into the angular momentum of the product molecule.

The H-atom elimination reaction is found to proceed through two transition-state structures, TS2 and TS3 (see Figure SI-1, Supporting Information, and Table 1). Although TS2 is energetically more favorable, a large majority of the trajectories react via the TS3 mechanism, as the bent O−C−H arrangement is sterically favored. We examined the trajectories occurring through the two mechanisms and found that the c.m. angular distributions demonstrated the expected trends; the TS2 trajectories led to more backward-scattered ethoxy products, with the OC_2H_5 departing in the opposite direction of the reagent O atom. The TS3 trajectories, on the other hand, resulted in more isotropic scattering, with a tendency for the OC_2H_5 product to be scattered in sideways directions. The average ethoxy scattering angles are 140 and 102° for the TS2 and TS3 trajectories, respectively, on the B3LYP surface with $E_{coll} = 90$ kcal mol^{-1}. The angular distributions for OC_2H_5 calculated for different collision energies (Figure SI-6, Supporting Information) indicate two peaks, at backward and sideways angles, at relatively low collision energies, but only a single peak in the sideways direction at higher collision energies. The energy partitioning in the products, however, did not seem to differ noticeably for the two mechanisms, with about 37% of the available energy going into translation and 63% into ethoxy internal modes, according to both the MSINDO and B3LYP calculations at $E_{coll} = 90$ kcal mol^{-1}. The fraction of the OC_2H_5 internal energy becomes smaller at lower collision energies, but it is still about half of the total energy at $E_{coll} = 60$ kcal mol^{-1}.

Whether or not the product detected at $m/z = 43$ is the primary OC_2H_5 or a secondary product such as CH_3CHO, the experimental excitation function (Figure 20) will correspond to the primary reaction, that is, H-atom elimination.[9] The experimentally determined relative excitation function has a similar shape as excitation functions calculated at MSINDO and B3LYP levels. The MSINDO excitation function required a shift of 25 kcal mol^{-1} to higher energy in order to provide agreement with the experimental and B3LYP results. This shift is similar to what was previously noted in analogous calculations for $O + CH_4$,[9] and it can be understood based on the low MSINDO barrier heights for TS2 and TS3 in Table 1 compared to more accurate results. The range of collision energies that were accessible in the experiment did not permit an experimental determination of the reaction threshold, as was accomplished in earlier experiments.[9,21,32] Nevertheless, extrapolation of the experimental excitation function would be consistent with the theoretically calculated barrier of 50.5 kcal mol^{-1}. Note that the barrier to H-atom elimination in the analogous reaction, $O(^3P) + CH_3 \rightarrow OCH_3 + H$, was found to be 45 kcal mol^{-1}.[9]

D. C−C Bond Breakage. The reaction $O(^3P) + CH_3CH_3 \rightarrow OCH_3 + CH_3$ was elusive in the experiment because no mass-to-charge ratio with evidence for this channel appears without interference from other ionizer fragments. Detailed analysis of the TOF distributions collected at $m/z = 29$ ($C_2H_5^+$, CHO^+) revealed the existence of signal that may be ascribed to OCH_3 from C−C bond breakage or to H_2CO from secondary dissociation of OC_2H_5. The latter is more likely because both theory and experiment suggest that H-atom elimination has a relatively high yield and will produce OC_2H_5 with enough internal energy to dissociate. Still, in order to determine an upper limit on the relative yield of C−C bond breakage, we made the assumption that unexplained signal at $m/z = 29$ came from OCH_3. This assumption led to a low relative yield, which is in general agreement with the theoretical results (see Table 2). However, it must be noted that the experimental data do not permit unambiguous assignment of any observed signal to the C−C bond-breakage reaction.

The dynamical information for this reaction pathway is therefore derived solely from the theoretical calculations. Similar to the H-atom elimination reaction, C−C bond breakage may occur through two different TS structures, corresponding to linear (TS4) and bent $O-C-CH_3$ (TS5) geometries. Trajectories across TS4 led largely to backward scattering of OCH_3, while those across TS5 produced a broad angular distribution of OCH_3 with a maximum in the sideways direction. Calculated angular distributions (Figure SI-7, Supporting Information) show the contributions from the two nominal pathways. The distribution calculated for the lowest collision energy, 60 kcal mol^{-1}, exhibits two maxima, with TS4 trajectories being responsible for scattering at the more backward angles and TS5 trajectories being responsible for the broad, sideways scattering. As the collision energy increases, the bimodality disappears, and the total distribution has a single maximum in the sideways direction. Further inspection of the energy disposal in the products showed a trend similar to that of H-atom abstraction;

about 80% of the available energy goes to translation, 15% into CH_3O internal modes, and only a small fraction into CH_3 internal excitation.

The TOF distributions collected at $m/z = 27$ were crucial to the identification of an additional signal at $m/z = 29$ that may arise from C−C breakage or secondary dissociation of OC_2H_5 because it was assumed that all of the signal components present in the $m/z = 27$ TOF distributions were also present in the $m/z = 29$ distributions. It should be pointed out that the C_2H_4 product of the theoretically predicted reaction, $O(^3P) + CH_3CH_3 \rightarrow H_2O + C_2H_4$, might also contribute to the signal at $m/z = 27$. We ignored this possibility in our analysis because we had no clear evidence for its existence. We observed no signal at $m/z = 18$ (H_2O^+), and all the other relevant mass-to-charge ratios (28, 27, 26, 25, and 24) had strong contributions from ionizer fragmentation of several obvious products. Given the detector background at $m/z = 18$ and the interference from many other products at $m/z = 24-28$, we cannot rule out the possibility that the reaction to produce $H_2O + C_2H_4$ occurred in the experiment. However, even if this reaction occurred, its relative yield must have been small, a few percent or less. Furthermore, our identification of the additional O-containing product at $m/z = 29$ would still be robust because the signal from this product was not present at $m/z = 27$, and the $m/z = 29$ signal could not have come from C_2H_4.

The existence of the C−C bond-breakage channel was reported in an earlier preliminary paper,[8] but the basis for this conclusion was flawed. The data presented in the earlier paper pertained to the reactions of O(^3P) with $CH_3CH_2CH_3$. An argument was made that the "fast" signal detected at short arrival times in the TOF distributions collected at $m/z = 29$ could only come from C−C bond breakage to form OCH_3 and CH_3CH_2. However, further experiments and in-depth analysis revealed that most of the signal at $m/z = 29$ that was assumed to arise from the OCH_3/CH_3CH_2 products was actually the result of $CH_3CH_2CH_3$ that scattered inelastically in the forward direction following low-impact-parameter collisions. Fragmentation of $CH_3CH_2CH_3$ in the ionizer produced signals at $m/z = 29$ and at several nearby mass-to-charge ratios. In collisions of O(^3P) with CH_3CH_3, which have been described here, the analogous inelastic scattering contribution has been discussed in connection with the $m/z = 27$ and 29 TOF distributions. The earlier arguments used for the example of O(^3P) collisions with $CH_3CH_2CH_3$ were in error because they did not consider the possibility of inelastic scattering of the alkane collision partner into the forward direction. As discussed above, the current detailed analysis only leads to the possibility that the C−C bond-breakage reaction may occur, and if it does, the relative yield must be less than ~6% of the reactive collisions (≤1% of all of the collisions).

VI. Concluding Remarks

The dynamics of collisions of hyperthermal O(^3P) with ethane were studied in detail by crossed molecular beams methods and by direct dynamics calculations. Four primary channels were studied, inelastic scattering, H-atom abstraction, H-atom elimination, and C−C bond breakage. Inelastic scattering occurred mainly through collisions with high-impact parameters, with very little loss of translational energy; these collisions led to forward scattering. Less probable, low-impact-parameter, inelastic collisions resulting in large losses in translational energy were also observed at sideways and backward c.m. angles. The H-atom abstraction reaction to form $OH + C_2H_5$ resulted in large releases of translational energy. The high translational energies are a consequence of a stripping mechanism that leads to forward scattering of the OH products. An H-atom elimination mechanism to form $OC_2H_5 + H$ was observed experimentally for the first time. Both theory and experiment found the ethoxy product to be scattered forward, sideways, and backward, with dips and maxima in the angular distribution. A large fraction of the available energy was transferred to the ethoxy product, which likely results in almost complete secondary dissociation of OC_2H_5 into $CH_3CHO + H$ and $H_2CO + CH_3$. The relative excitation function of the H-atom elimination reaction was also measured and agreed well with theoretical calculations. The experiment suggests that the upper limit to the reaction barrier of this channel is ~60 kcal mol^{-1}, while theory locates the barrier at 50.5 kcal mol^{-1}. The C−C bond-breakage channel to form $OCH_3 + CH_3$ was identified in the theoretical calculations, but it could not be identified unambiguously in the experiment. The calculations predict low product translational energies (~20% of the available energy) and mainly sideways scattering of OCH_3. Experiment and theory are in good agreement on the relative yields of all of the channels. The dominant reactive pathway is H-atom abstraction followed by a substantial fraction of H-atom elimination. C−C bond breakage might occur, but it accounts for less than 6% of reactive collisions. Theory predicts another product channel (H_2O + $^3CH_3CH$) with a similar yield to C−C bond breakage, but this channel could not be identified in the experiment.

Acknowledgment. This work was supported by the Air Force Office of Scientific Research (F49620-01-1-0276, F49620-01-1-0335, FA9550-07-1-0095), the Small Business Innovative Research (SBIR) program of the Missile Defense Agency (F04611-03-C-0015), and the Missile Defense Agency under Cooperative Agreement HQ0006-05-2-0001.

Supporting Information Available: Theoretically calculated transition-state structures, excitation functions, opacity functions, and angular distributions. Representative time-of-flight distributions collected at a variety of mass-to-charge ratios. This material is available free of charge via the Internet at http://pubs.acs.org.

References and Notes

(1) Casavecchia, P.; Leonori, F.; Balucani, N.; Petrucci, R.; Capozza, G.; Segoloni, E. *Phys. Chem. Chem. Phys.* **2009**, *11*, 46.

(2) Ausfelder, F.; McKendrick, K. G. *Prog. React. Kinet. Mech.* **2000**, *25*, 299.

(3) Murad, E. *J. Spacecr. Rockets* **1996**, *33*, 131.

(4) Troya, D.; Schatz, G. C. *Int. Rev. Phys. Chem.* **2004**, *23*, 341.

(5) Zhang, J.; Garton, D. J.; Minton, T. K. *J. Chem. Phys.* **2002**, *117*, 6239.

(6) Zhang, J.; Upadhyaya, H. P.; Brunsvold, A. L.; Minton, T. K. *J. Phys. Chem. B* **2006**, *110*, 12500.

(7) Kim, D; Schatz, G. C. *J. Phys. Chem. A* **2007**, *111*, 5019.

(8) Garton, D. J.; Minton, T. K.; Troya, D.; Pascual, R.; Schatz, G. C. *J. Phys. Chem. A* **2003**, *107*, 4583.

(9) Troya, D.; Schatz, G. C.; Garton, D. J.; Brunsvold, A. L.; Minton, T. K. *J. Chem. Phys.* **2004**, *120*, 731.

(10) Gindulyte, A.; Massa, L.; Banks, B. A.; Rutledge, S. K. *J. Phys. Chem. A* **2000**, *104*, 9976.

(11) Troya, D.; Pascual, R. Z.; Garton, D. J.; Minton, T. K.; Schatz, G. C. *J. Phys. Chem. A* **2003**, *107*, 7161.

(12) Yan, T.; Doubleday, C.; Hase, W. L. *J. Phys. Chem. A* **2004**, *108*, 9863.

(13) (a) Ahlswede, B.; Jug, K. *J. Comput. Chem.* **1999**, *20*, 563. (b) Jug, K.; Geudtner, G.; Homann, T. *J. Comput. Chem.* **2000**, *21*, 974. (c) Bredow, T.; Geudtner, G.; Jug, K. *J. Comput. Chem.* **2001**, *22*, 89.

(14) (a) Becke, A. D. *J. Chem. Phys.* **1993**, *98*, 5648. (b) Lee, C.; Yang, W.; Parr, R. G. *Phys. Rev. B* **1988**, *37*, 785.

(15) Yan, T.; Hase, W. L.; Doubleday, C. *J. Chem. Phys.* **2004**, *120*, 9253.

(16) Kong, J.; White, C. A.; Krylov, A. I.; Sherrill, C. D.; Adamson, R. D.; Furlani, T. R.; Lee, M. S.; Lee, A. M.; Gwaltney, S. R.; Adams,

T. R.; Ochsenfeld, C.; Gilbert, A. T. B.; Kedziora, G. S.; Rassolov, V. A.; Maurice, D. R.; Nair, N.; Shao, Y.; Besley, N. A.; Maslen, P. E.; Dombroski, J. P.; Dachsel, H.; Zhang, W. M.; Korambath, P. P.; Baker, J.; Byrd, E. F. C.; Van Voorhis, T.; Oumi, M.; Hirata, S.; Hsu, C. P.; Ishikawa, N.; Florian, J.; Warshel, A.; Johnson, B. G.; Gill, P. M. W.; Head-Gordon, M.; Pople, J. A. *Q-Chem*, Version 2.0; Q-Chem, Inc., Export, PA 2000.

(17) *Numerical Recipes in FORTRAN: The Art of Scientific computing*. 2nd ed.; Press, W. H.; Flannery, B. P.; Teukolsky, S. A.; Vetterling, W. T. Cambridge University Press: Cambridge, U.K., and New York, 1992.

(18) Garton, D. J.; Brunsvold, A. L.; Minton, T. K.; Troya, D.; Maiti, B.; Schatz, G. C. *J. Phys. Chem. A* **2006**, *110*, 1327.

(19) Brunsvold, A. L.; Upadhyaya, H. P.; Zhang, J.; Cooper, R.; Minton, T. K.; Braunstein, M.; Duff, J. W. *J. Phys. Chem. A* **2008**, *112*, 2192.

(20) Proch, D.; Trickl, T. *Rev. Sci. Instrum.* **1989**, *60*, 713.

(21) Garton, D. J.; Minton, T. K.; Maiti, B.; Troya, D.; Schatz, G. C. *J. Chem. Phys.* **2003**, *118*, 1585.

(22) The study reported in ref 9 led to the conclusion that any O_2 in the hyperthermal O/O_2 beam must be in the ground $^3\Sigma_g^-$ state because the experiment was not able to identify an H_2O product, which was predicted by theory to be indicative of an $O_2(^1\Delta)$ reaction, $O_2(^1\Delta) + CH_4 \rightarrow H_2O + H_2CO$.

(23) Caledonia, G. E.; Krech, R. H.; Green, D. B. *AIAA J.* **1987**, *25*, 59.

(24) Brink, G. O. *Rev. Sci. Instrum.* **1966**, *37*, 857.

(25) Daly, N. R. *Rev. Sci. Instrum.* **1960**, *31*, 264.

(26) Lee, Y. T. Reactive Scattering I: Nonoptical Methods. In *Atomic and Molecular Beam Methods*; Scoles, G., Ed.; Oxford University Press: New York, 1988; Vol. 1, pp 553−568.

(27) Buss, R. J. Ph.D. Thesis, University of California, Berkeley, CA, 1979.

(28) Zhao, X. Ph.D. Thesis, University of California, Berkeley, CA, 1988.

(29) Zhang, J. Ph.D. Thesis, Montana State University, Bozeman, MT, 2001.

(30) Lin, J. J.; Lee, Y. T.; Yang, X. *J. Chem. Phys.* **1998**, *109*, 2975.

(31) Blank, D. A.; Hemmi, N.; Suits, A. G.; Lee, Y. T. *Chem. Phys.* **1998**, *231*, 261.

(32) Brunsvold, A. L.; Garton, D. J.; Minton, T. K.; Troya, D.; Schatz, G. C. *J. Chem. Phys.* **2004**, *121*, 11702.

(33) Brunsvold, A. L.; Zhang, J.; Upadhyaya, H. P.; Minton, T. K.; Camden, J. P.; Paci, J. T.; Schatz, G. C. *J. Phys. Chem. A* **2007**, *111*, 10907.

(34) Hoyermann, K.; Olzmann, M.; Seeba, J.; Viskolcz, *J. Phys. Chem. A* **1999**, *103*, 5692.

(35) (a) Chase, M. W.; Davies, C. A.; Downey, J. R.; Frurip, D. J.; McDonald, R. A.; Syverud, A. N., JANAF Thermochemical Tables, 3rd ed. *J. Phys. Chem. Ref. Data* **1985**, *14*, Suppl. No. 1. (b) Gurvich, L. V., Veyts, I. V., Alcock, C. B., Eds. *Thermodynamic Properties of Individual Substances*, 4th ed.; Hemisphere: New York, 1989.

(36) CCSD(T)/cc-pVTZ values from ref 11 corrected for zero-point energies.

(37) (a) Ruscic, B.; Wagner, A. F.; Harding, L. B.; Asher, R. L.; Feller, D.; Dixon, D. A.; Peterson, K. A.; Song, Y.; Qian, X. M.; Ng, C. Y.; Liu, J. B.; Chen, W. W. *J. Phys. Chem. A* **2002**, *106*, 2727. (b) Marshall, P. *J. Phys. Chem. A* **1999**, *103*, 4560.

(38) Berkowitz, J.; Ellison, G. B.; Gutman, D. *J. Phys. Chem.* **1994**, *98*, 2744; JANAF Thermochemical Tables.

(39) Hippler, H.; Striebel, F.; Viskolcz, B. *Phys. Chem. Chem. Phys.* **2001**, *3*, 2450.

(40) Dertinger, S.; Geers, A.; Kappert, J.; Wiebrecht, J.; Temps, F. *Faraday Discuss.* **1996**, *102*, 31.

(41) Caralp, F.; Devolder, P.; Fittschen, C.; Gomez, N.; Hippler, H.; Mereau, R.; Rayez, M. T.; Striebel, F.; Viskolcz, B. *Phys. Chem. Chem. Phys.* **1999**, *1*, 2935.

(42) da Silva, G.; Bozzelli, J. W. *J. Phys. Chem. A* **2006**, *110*, 13058; corrected for 0 K.

(43) Marenich, A. V.; Boggs, J. E. *J. Chem. Phys.* **2003**, *119*, 10105.

JP900412W